

Analysis Note:

**Measurement of system size dependence of
directed flow of protons (anti-protons) at
RHIC**

Muhammad Farhan Taseer

mfarhan_taseer@impcas.ac.cn

Target journal: **Physics Review Letters**

2025 年 3 月 25 日



Abstract

The directed flow (v_1) is a sensitive probe of the initial state conditions in heavy-ion collisions. One key initial condition is the presence of an extremely strong electromagnetic field, which induces charge splitting between particles and antiparticles. Another crucial aspect is the deposition of baryon charge, which can be specifically probed through the directed flow of baryons, offering insights into baryon transport within Quark-Gluon Plasma (QGP) [1]. In this work, we present the rapidity dependent directed flow (v_1) and its slope (dv_1/dy) for π^\pm , K^\pm and $p(\bar{p})$ as a function of centrality in Au+Au and Isobar (Ru+Ru and Zr+Zr) collisions at $\sqrt{s_{NN}} = 200$ GeV, and in U+U collisions at $\sqrt{s_{NN}} = 193$ GeV, as measured by the STAR experiment at RHIC. The slope (dv_1/dy) for $p(\bar{p})$ and the charge dependent difference $\Delta(dv_1/dy)$ exhibit a clear system size dependence, with an ordering of U+U > Au+Au > Isobar (Ru+Ru and Zr+Zr), while the total baryons ($p + \bar{p}$) remain independent of system size. This is the first observation of the system size dependence for v_1 and $\Delta(dv_1/dy)$ of baryons. In contrast, the inclusive particles, particularly mesons (π^\pm and K^\pm), show no dependence on system size, consistent with previous findings at RHIC [2]. The $\Delta(dv_1/dy)$ pattern for protons is primarily influenced by baryon transport and electromagnetic fields. In the most central collisions, where the electromagnetic field is minimal, baryon transport can be assessed more clearly. Additionally, in mid-central and peripheral collisions, these data can provide insights into the strength of electromagnetic fields and the conductivities of the medium [3].



Contents

1.1 Introduction	1
1.2 Dataset and Event Selection	2
1.2.1 Dataset	2
1.2.2 Events Selection	2
1.2.3 Centrality Definition	4
1.3 Event Plane Reconstruction	4
1.3.1 Event Plane Resolution	5
1.4 Particle Reconstruction	6
1.4.1 Track Selection	6
1.4.2 Particle Identification	6
1.5 Analysis Procedure	7
1.6 Charge-dependent directed flow in U+U collisions at $\sqrt{s_{NN}} = 193$ GeV	8
1.6.1 Directed flow of π^\pm meson	8
1.6.2 Directed flow of K^\pm meson	13
1.6.3 Directed flow of p and \bar{p}	18
1.7 Systematic Uncertainties Evaluation	23
1.7.1 Systematic Uncertainty of v_1 as a function of rapidity	24
1.7.2 Systematic Uncertainty of dv_1/dy as a function of centrality	30
1.7.3 Systematic Uncertainty of $\Delta(dv_1/dy)$ as a function of centrality ..	33
1.7.4 Systematic Uncertainty of v_1 as a function of p_T	35
1.8 Comparison of directed flow in U+U collisions at $\sqrt{s_{NN}} = 193$ GeV to Au+Au and Isobar (Ru+Ru and Zr+Zr) data at $\sqrt{s_{NN}} = 200$ GeV ..	41
1.8.1 Directed flow of π^\pm in U+U, Au+Au and Isobar collisions	41
1.8.2 Directed flow of K^\pm in U+U, Au+Au and Isobar collisions	43
1.8.3 Directed flow of p and \bar{p} in U+U, Au+Au and Isobar collisions ..	45
1.9 Summary and Conclusion	50



List of Figures

Figure 1-1 Distribution of reconstructed vertex v_z (left panel), $v_r = \sqrt{v_x^2 + v_y^2}$ (right panel) and the difference $ V_{z,TPC} - V_{z,VPD} $ (bottom panel) after event cuts.	3
Figure 1-2 Event plane distribution before and after shift correction.	5
Figure 1-3 Event plane resolution as a function of centrality.	5
Figure 1-4 The ionization energy loss dE/dx (left panel) of charged particles as a function of momentum in TPC and mass-squared (right panel) as a function of momentum in TOF	7
Figure 1-5 Directed flow of π^+ (red solid circles) and π^- (blue open circles) as a function of rapidity at 193 GeV U+U collisions. From top left to bottom right, centrality changes from peripheral to central.	9
Figure 1-6 $a_1 = \langle \sin(\phi - \Psi) \rangle$ of π^+ (red solid squares) and π^- (blue open squares) as a function of rapidity at 193 GeV U+U collisions. From top left to bottom right, centrality changes from peripheral to central.	10
Figure 1-7 The slope (dv_1/dy) of π^+ (red solid circles) and π^- (blue solid circles) as a function of centrality at 193 GeV U+U collisions.	11
Figure 1-8 The Δv_1 and Δa_1 slopes between π^+ and π^- as a function of centrality at 193 GeV U+U collisions. The Δa_1 slope is shown as benchmark.	11
Figure 1-9 v_1 as a function of p_T between π^+ and π^- at 193 GeV U+U collisions. The solid pink marker represents π^+ and the open black marker stands for π^-	12
Figure 1-10 The Δv_1 as a function of p_T for pion at 193 GeV U+U collisions. The pink marker is used for 10-40% centrality and the black marker represents 40-80% centrality	12
Figure 1-11 Directed flow of K^+ (red solid circles) and K^- (blue open circles) as a function of rapidity at 193 GeV U+U collisions. From top left to bottom right, centrality changes from peripheral to central.	14
Figure 1-12 $a_1 = \langle \sin(\phi - \Psi) \rangle$ of K^+ (red solid circles) and K^- (blue open circles) as a function of rapidity at 193 GeV U+U collisions. From top left to bottom right, centrality changes from peripheral to central.	15
Figure 1-13 The slope (dv_1/dy) of K^+ (red solid circles) and K^- (blue solid circles) as a function of rapidity at 193 GeV U+U collisions.	16
Figure 1-14 The Δv_1 and Δa_1 slopes between K^+ and K^- as a function of centrality at 193 GeV U+U collisions. The Δa_1 slope is shown as benchmark.	16

Figure 1-15 v_1 as a function of p_T between K^+ and K^- at 193 GeV U+U collisions. The solid pink marker represents K^+ and the open black marker stands for K^-	17
Figure 1-16 The Δv_1 as a function of p_T for kaon at 193 GeV U+U collisions. The pink marker is used for 10-40% centrality and the black marker represents 40-80% centrality	17
Figure 1-17 Directed flow of p (red solid circles) and \bar{p} (blue open circles) as a function of rapidity at 193 GeV U+U collisions. From top left to bottom right, centrality changes from peripheral to central.	19
Figure 1-18 $a_1 = \langle \sin(\phi - \Psi) \rangle$ of p (red solid circles) and \bar{p} (blue open circles) as a function of rapidity at 193 GeV U+U collisions. From top left to bottom right, centrality changes from peripheral to central.	20
Figure 1-19 The slope (dv_1/dy) of p (red solid circle) and \bar{p} (blue solid circles) as a function of centrality at 193 GeV U+U collisions.	21
Figure 1-20 The Δv_1 and Δa_1 slopes between p and \bar{p} as a function of centrality at 193 GeV U+U collisions. The Δa_1 slope is shown as benchmark.	21
Figure 1-21 v_1 as a function of p_T between p and \bar{p} at 193 GeV U+U collisions. The solid pink marker represents p and the open black marker stands for \bar{p}	22
Figure 1-22 The Δv_1 as a function of p_T for proton at 193 GeV U+U collisions. The pink marker is used for 10-40% centrality and the black marker represents 40-80% centrality	22
Figure 1-23 v_1 of π^+ for various systematic cuts (left panel) and the systematic/statistical error (right panel) in 10-40% centrality.	24
Figure 1-24 v_1 of π^+ for various systematic cuts (left panel) and the systematic/statistical error (right panel) in 40-80% centrality.	25
Figure 1-25 v_1 of π^- for various systematic cuts (left panel) and systematic/statistical error (right panel) in 10-40% centrality.	25
Figure 1-26 v_1 of π^- for various systematic cuts (left panel) and systematic/statistical error (right panel) in 40-80% centrality.	26
Figure 1-27 v_1 of K^+ for various systematic cuts (left panel) and the systematic/statistical error (right panel) in 10-40% centrality.	26
Figure 1-28 v_1 of K^+ for various systematic cuts (left panel) and the systematic/statistical error (right panel) in 40-80% centrality.	27
Figure 1-29 v_1 of K^- for various systematic cuts (left panel) and the systematic/statistical error (right panel) in 10-40% centrality.	27
Figure 1-30 v_1 of K^- for various systematic cuts (left panel) and the systematic/statistical error (right panel) in 40-80% centrality.	28
Figure 1-31 v_1 of p for various systematic cuts (left panel) and the systematic/statistical error (right panel) in 10-40% centrality.	28

Figure 1-32 v_1 of p for various systematic cuts (left panel) and the systematic/statistical error (right panel) in 40-80% centrality.	29
Figure 1-33 v_1 of \bar{p} for various systematic cuts (left panel) and the systematic/statistical error (right panel) in 10-40% centrality.	29
Figure 1-34 v_1 of \bar{p} for various systematic cuts (left panel) and the systematic/statistical error (right panel) in 40-80% centrality.	30
Figure 1-35 The slope (dv_1/dy) of π^+ for various systematic cuts (left panel) and the systematic/statistical error (right panel).	30
Figure 1-36 The slope (dv_1/dy) of π^- for various systematic cuts (left panel) and the systematic/statistical error (right panel).	31
Figure 1-37 The slope (dv_1/dy) of K^+ for various systematic cuts (left panel) and the systematic/statistical error (right panel).	31
Figure 1-38 The slope (dv_1/dy) of K^- for various systematic cuts (left panel) and systematic/statistical error (right panel).	32
Figure 1-39 The slope (dv_1/dy) of p for various systematic cuts (left panel) and the systematic/statistical error (right panel)	32
Figure 1-40 The slope (dv_1/dy) of \bar{p} for various systematic cuts (left panel) and the systematic/statistical error (right panel).	33
Figure 1-41 The $\Delta(dv_1/dy)$ of pion for various systematic cuts (left panel) and the systematic/statistical error (right panel).	33
Figure 1-42 The $\Delta(dv_1/dy)$ of kaon for various systematic cuts (left panel) and the systematic/statistical error (right panel).	34
Figure 1-43 The $\Delta(dv_1/dy)$ of proton for various systematic cuts (left panel) and the systematic/statistical error (right panel).	34
Figure 1-44 $v_1(p_T)$ of π^+ for various systematic cuts (left panel) and the systematic/statistical error (right panel) in 10-40% centrality.	35
Figure 1-45 $v_1(p_T)$ of π^+ for various systematic cuts (left panel) and the systematic/statistical error (right panel) in 40-80% centrality.	35
Figure 1-46 $v_1(p_T)$ of π^- for various systematic cuts (left panel) and the systematic/statistical error (right panel) in 10-40% centrality.	36
Figure 1-47 $v_1(p_T)$ of π^- for various systematic cuts (left panel) and the systematic/statistical error (right panel) in 40-80% centrality.	36
Figure 1-48 $v_1(p_T)$ of K^+ for various systematic cuts (left panel) and the systematic/statistical error (right panel) in 10-40% centrality.	37
Figure 1-49 $v_1(p_T)$ of K^+ for various systematic cuts (left panel) and the systematic/statistical error (right panel) in 40-80% centrality.	37
Figure 1-50 $v_1(p_T)$ of K^- for various systematic cuts (left panel) and the systematic/statistical error (right panel) in 10-40% centrality.	38

Figure 1-51 $v_1(p_T)$ of K^- for various systematic cuts (left panel) and the systematic/statistical error (right panel) in 40-80% centrality.	38
Figure 1-52 $v_1(p_T)$ of p for various systematic cuts (left panel) and the systematic/statistical error (right panel) in 10-40% centrality.	39
Figure 1-53 $v_1(p_T)$ of p for various systematic cuts (left panel) and the systematic/statistical error (right panel) in 40-80% centrality.	39
Figure 1-54 $v_1(p_T)$ of \bar{p} for various systematic cuts (left panel) and the systematic/statistical error (right panel) in 10-40% centrality.	40
Figure 1-55 $v_1(p_T)$ of \bar{p} for various systematic cuts (left panel) and the systematic/statistical error (right panel) in 40-80% centrality.	40
Figure 1-56 The event plane resolution as a function of centrality in U+U, Au+Au and Isobar (Ru+Ru and Zr+Zr) collisions at 193 and 200 GeV. The red marker is used for U+U, the blue marker is for Au+Au and the green marker stands for the resolution values in isobar data.	41
Figure 1-57 Comparison of directed flow of π^+ (left panel) and π^- (right panel) measured in this work with the published Au+Au and Isobar data at 200 GeV for 10-40% centrality.	42
Figure 1-58 Comparison of slope (dv_1/dy) of π^+ (left panel) and π^- (right panel) measured in this work with the published Au+Au and Isobar data at 200 GeV.	42
Figure 1-59 Comparison of $\Delta(dv_1/dy)$ of pion measured in this work with the published Au+Au and Isobar data at 200 GeV.	43
Figure 1-60 Comparison of directed flow of K^+ (left panel) and K^- (right panel) measured in this work with the published Au+Au and Isobar data at 200 GeV for 10-40% centrality.	43
Figure 1-61 Comparison of dv_1/dy of K^+ (left panel) and K^- (right panel) measured in this work with the published Au+Au and Isobar data at 200 GeV.	44
Figure 1-62 Comparison of $\Delta(dv_1/dy)$ of kaon measured in this work with the published Au+Au and Isobar data at 200 GeV.	44
Figure 1-63 Comparison of directed flow of p (left panel) and \bar{p} (right panel) measured in this work with the published Au+Au and Isobar data at 200 GeV for 10-40% centrality.	45
Figure 1-64 Comparison of dv_1/dy of p (left panel) and \bar{p} (right panel) measured in this work with the published Au+Au and Isobar data at 200 GeV.	46
Figure 1-65 Comparison of $\Delta(dv_1/dy)$ of proton measured in this work with the published Au+Au and Isobar data at 200 GeV.	46

- Figure 1-66 Plots show the directed flow (v_1) for π^\pm , K^\pm and $p(\bar{p})$ as a function of rapidity in U+U collisions at 193 GeV, Au+Au and Isobar (Ru+Ru and Zr+Zr) collisions at 200 GeV in 10-40% centrality. The red marker is used for U+U, green marker is for Au+Au and blue marker represents Isobar data. The shaded bands indicate systematic uncertainties. 47
- Figure 1-67 Plots show the slope (dv_1/dy) for π^\pm , K^\pm and $p(\bar{p})$ as a function of centrality in U+U collisions at 193 GeV, Au+Au and Isobar (Ru+Ru and Zr+Zr) collisions at 200 GeV. Slopes are obtained by fitting v_1 in $-0.8 < y < 0.8$ using a linear function. The red marker is used for U+U, black marker is for Au+Au and blue marker represents Isobar data. The Solid black and blue lines are the default hydro (inhomogeneous baryon distribution) model results for Au+Au and Isobar data respect. The shaded bands indicate systematic uncertainties. 48
- Figure 1-68 Plots show $\Delta(dv_1/dy)$ and $\Sigma(dv_1/dy)$ for π^\pm , K^\pm and $p(\bar{p})$ as a function of centrality in U+U collisions at 193 GeV, Au+Au and Isobar (Ru+Ru and Zr+Zr) collisions at 200 GeV. The red marker is used for U+U, green marker is for Au+Au and blue marker represents Isobar data. The Solid green and blue lines are the default hydro (inhomogeneous baryon distribution) model results for Au+Au and Isobar data. The dashed green line, in proton Δv_1 and Σv_1 , is a special case in which Au+Au hydro is run with net baryon same as Ru+Ru at a fixed $\langle N_{part} \rangle$. The shaded bands indicate systematic uncertainties. 49

List of Tables

Table 1-1 Dataset of U+U collisions at $\sqrt{s_{NN}} = 193$ GeV	2
Table 1-2 PID cuts for U+U collisions at $\sqrt{s_{NN}} = 193$ GeV.	6
Table 1-3 The sources of systematic uncertainties in U+U collisions at $\sqrt{s_{NN}} = 193$ GeV	23

1.1 Introduction

An ultra-strong magnetic field ($B \approx 10^{18}$ Gauss) is anticipated during the early stages of heavy ion collisions. The magnetic field is primarily generated by spectators and can cause charge splitting between particles and antiparticles under the influence of various electromagnetic (EM) effects present in the expanding quark-gluon plasma (QGP), like Hall effect (due to Lorentz force $\mathbf{F} = q\mathbf{v} \times \mathbf{B}$), Coulomb effect (\mathbf{E} generated by spectator nucleons) and a time dependent effect called Faraday Induction (decrease in \mathbf{B} as spectators fly away) [4, 5]. As a result, a net current flows in the medium (QGP) called directed flow (v_1).

The directed flow or the first harmonic flow coefficient (v_1) describes collective sideward motion of produced particles and nuclear fragments, and carries information from the very early stages of collision [6]. Specifically, particles and antiparticles with opposite charges experience different contributions to their rapidity-odd directed flow, $v_1(y)$ [3]. The $\Delta(dv_1/dy)$, difference in v_1 slope between positive and negative charged particles, can be used to investigate electromagnetic field effects in heavy-ion collisions. Moreover, positive $\Delta(dv_1/dy)$ refers to the dominance of Hall effect in central collisions, whereas the negative $\Delta(dv_1/dy)$, in peripheral collisions, is primarily due to Faraday induction combined with the Coulomb effect [4, 5]. Another important clue of v_1 splitting (based on model studies [7–9]) is the transported quarks effect which states that the quarks transported from colliding nuclei to mid-rapidity regions and the quarks produced in the final state may have different contributions due to differences in their quark compositions, resulting a charge dependent $v_1(y)$ and $\Delta(dv_1/dy)$ [3].

This analysis is the first report on system size dependence of directed flow (v_1) in heavy ion collisions at the STAR experiment of RHIC. In this report, We shall present the analysis details of directed flow (v_1) of the three identified particles π^\pm , K^\pm and $p(\bar{p})$ in Run12 U+U collisions at $\sqrt{s_{NN}} = 193$ GeV. The splitting of v_1 between positive and negative charged particles is measured as a function of rapidity and centrality. Additionally, v_1 and $\Delta(dv_1/dy)$ measured in this work is also compared with published results in Au+Au and isobar collisions at $\sqrt{s_{NN}} = 200$ GeV [3]. These findings provide constraints on initial electromagnetic fields and offer means to understand baryon deposition and baryon transport mechanism at various system sizes.

1.2 Dataset and Event Selection

1.2.1 Dataset

The data analyzed in this report is recorded by the STAR experiment at Relativistic Heavy Ion Collider (RHIC) in the year 2012 for U+U collisions at $\sqrt{s_{NN}} = 193$ GeV. The dataset consist of information about each Uranium (U^{238}) on Uranium (U^{238}) collision, known as events. The events are stored in microDST files for the purpose of physics analysis and contain all the information of recorded data like trigger information, signals from the recorded detector sub-systems and track details such as the momentum vectors of the particles produced in each event. The details of the dataset are listed as:

Table 1-1 Dataset of U+U collisions at $\sqrt{s_{NN}} = 193$ GeV

Data	Tag	Library	Stream	Trigger ID
U+U, 193 GeV	P12id	SL22a	st_physics	400005, 400015 400025, 400035

1.2.2 Events Selection

The events are stored in microDST files with each file representing a single 'run'. A total of 783 runs are analyzed in this analysis. The details of events selection is summarized as:

- primary vertex along beam direction $|V_z| \leq 50$ cm
- primary vertex in transverse direction $|V_r| \leq 2$ cm
- difference between vertex in TPC and in VPD $|V_{z,TPC} - V_{z,VPD}| \leq 3$ cm

In addition, 19 bad runs are also excluded from this analysis based on the quality assurance (QA) check of the data at <https://drupal.star.bnl.gov/STAR/blog/yezhenyu/nbinary-and-npart-uu-collisions-zhenyu>. Finally, a total of 250 million good quality minimum-bias triggered events are analyzed in analysis after applying all the event cuts.

List of bad runs: 13117026, 13117027, 13117028, 3117029, 13117030, 13117031, 13117032, 13117033, 13117034, 13117035, 13117036, 13118009, 13118034, 13118035, 13119016, 13119017, 13129047, 13129048, 13132047.

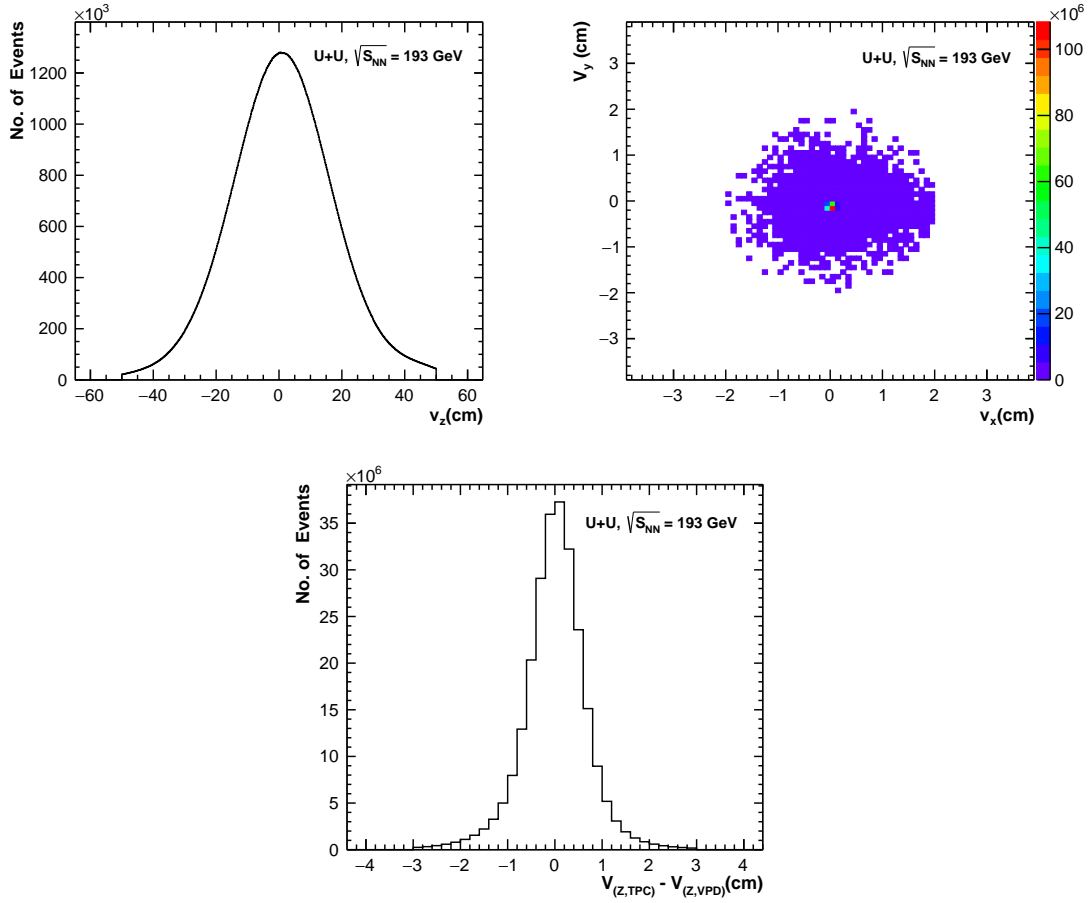


Figure 1-1 Distribution of reconstructed vertex v_z (left panel), $v_r = \sqrt{v_x^2 + v_y^2}$ (right panel) and the difference $|V_{z,TPC} - V_{z,VPD}|$ (bottom panel) after event cuts.

1.2.3 Centrality Definition

Centrality is the measure of impact parameter (b) and define as the degree of overlap between two nuclei. The impact parameter is the shortest distance between the center of two colliding nuclei. Since it cannot be measured directly, therefore centrality of the collision is determined using the multiplicity of primary charged particles. In this analysis, the minimum bias good events are divided into 9 centrality classes: (0 – 5%, 5 – 10%, 10 – 20%, 20 – 30%, 30 – 40%, 40 – 50%, 50 – 60%, 60 – 70%, 70 – 80%). This selection is based on the StRefMultCorr class which is specially designed for the STAR data and can be found at <http://www.star.bnl.gov/protected/common/common2010/centrality/index.html>.

1.3 Event Plane Reconstruction

The reaction plane is defined by beam axis (z -axis) and the impact parameter (b). The estimated reaction plane (derived from the particles produced in the collision) is known as event plane. However, the distribution of event plan is not uniform between 0 and 2π due to imperfect azimuthal symmetry (such as sector boundaries between ZDC-SMD, non-uniform efficiency, temporarily dead channels, etc.), and can bias flow results if not corrected. Therefore, the event plane is corrected by applying various methods like phi weight, re-centering and shift correction. In this analysis, the first order event plane (Ψ_1^{ZDC}) is reconstructed using ZDC detector and the event plan is flatten by applying Shift correction using the following function:

$$\Psi' = \Psi + \sum_{i=1}^{20} \frac{2}{i} (-\langle \sin(i\Psi) \rangle \cos(i\Psi) + \langle \cos(i\Psi) \rangle \sin(i\Psi)) \quad (1-1)$$

The angle brackets $\langle \rangle$ in the above equation represents the average over a large number of events. The reasonable flat distribution of event plane is obtained after calculating the correction term several times. In this analysis, we use up to the 20th harmonic to flatten the event plane angle distribution. Figure 1.2 shows uncorrected, and shift corrected event plane distributions.

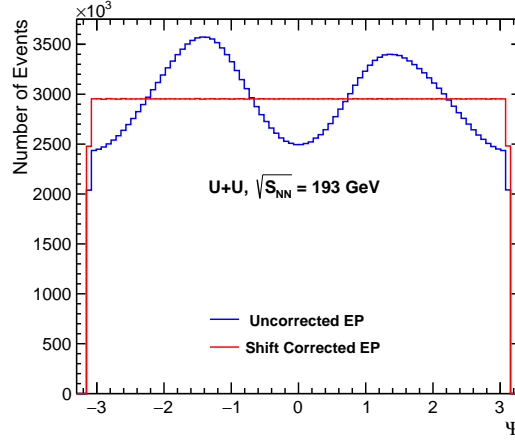


Figure 1-2 Event plane distribution before and after shift correction.

1.3.1 Event Plane Resolution

The event plane resolution is determined in order to remove the variations in the estimated event plane which may be due to the finite number of particles. In this analysis, the following Bessel function is used to calculate the resolution values of the first order event plane (Ψ_1^{ZDC}).

$$R_\Psi = \frac{\sqrt{\pi}}{2\sqrt{2}} \chi \exp\left(-\frac{\chi^2}{4}\right) \left[I_0\left(\frac{\chi^2}{4}\right) + I_1\left(\frac{\chi^2}{4}\right) \right] \quad (1-2)$$

where X can be determined from sub-event plane resolution. The resolution values for 9 different centrality classes 0 – 5%, 5 – 10%, 10 – 20%, 20 – 30%, 30 – 40%, 40 – 50%, 50 – 60%, 60 – 70%, 70 – 80% are 0.145016, 0.248548, 0.345383, 0.414196, 0.444727, 0.448302, 0.428285, 0.385058, 0.328569 respectively.

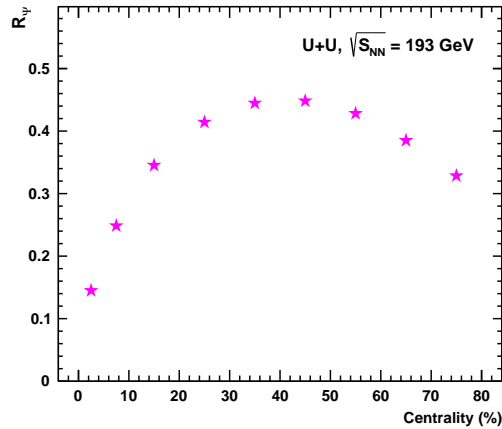


Figure 1-3 Event plane resolution as a function of centrality.

1.4 Particle Reconstruction

1.4.1 Track Selection

The Time Projection Chamber (TPC) of STAR is used for charged particle tracking within $|\eta| < 1$ and provides full 2π azimuthal coverage. Both primary and global tracks are considered in this analysis. The general criteria of track selection is as follows:

- All the tracks must be within a pseudo-rapidity range of ($\eta \leq 1.0$)
- The distance of closest approach (DCA) for all tracks ($DCA \leq 3$ cm)
- All tracks must have a minimum number of 15 fit points in the TPC ($nHits \leq 15$)

1.4.2 Particle Identification

The charged particles are identified by utilizing Time Projection Chamber (TPC) and Time of Flight (TOF) detectors. The TPC of STAR is capable to measure and reconstruct the momentum of charged particles based on their ionization energy loss (dE/dx). For all the charged particles, we required that the standard deviation of the measured (dE/dx) is less than 2σ from the expected (dE/dx) value. Mathematically,

$$n\sigma \propto \ln \left(\frac{\langle dE/dx \rangle_{\text{measured}}}{\langle dE/dx \rangle_{\text{expectation}}} \right) \quad (1-3)$$

The purity of charged particles is ensured by applying TOF detector which provides the mass square information of particles based on their time-of-flight and momentum measurements. A lower p_t cut and an upper p cut is applied for each particle to differentiate between different charged particles. The general criteria of particle identification is summarized in table 1.2:

Table 1-2 PID cuts for U+U collisions at $\sqrt{s_{NN}} = 193$ GeV.

π^\pm	$ n\sigma < 2.0$	$-0.01 < m^2 < 0.10$ (GeV/c ²) ²	$p_t > 0.2$ GeV/c & $p < 1.6$ GeV/c
K^\pm	$ n\sigma < 2.0$	$0.20 < m^2 < 0.35$ (GeV/c ²) ²	$p_t > 0.2$ GeV/c & $p < 1.6$ GeV/c
$p(\bar{p})$	$ n\sigma < 2.0$	$0.80 < m^2 < 1.0$ (GeV/c ²) ²	$p_t > 0.4$ GeV/c & $p < 2.0$ GeV/c

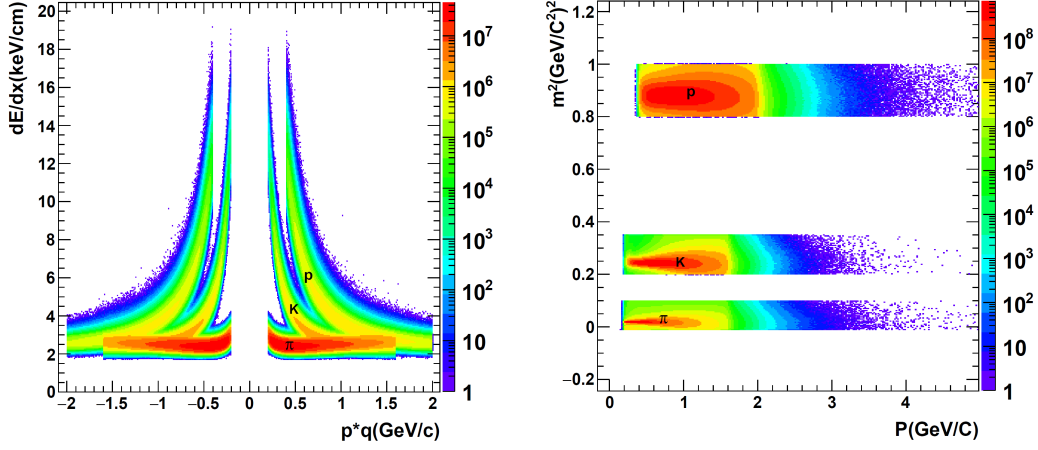


Figure 1-4 The ionization energy loss dE/dx (left panel) of charged particles as a function of momentum in TPC and mass-squared (right panel) as a function of momentum in TOF

1.5 Analysis Procedure

In heavy ion collisions, anisotropic flow is the measure of the Fourier expansion of Azimuthal distributions of produced particles with respect to reaction plane and can be written as:

$$E \frac{d^3 N}{d^3 p} = \frac{1}{2\pi} \frac{d^2 N}{p_T d p_T dy} \left(1 + \sum_{n=1}^{\infty} 2v_n \cos(\phi - \Psi) \right) \quad (1-4)$$

The directed (v_1) is the first harmonic flow coefficient in the above equation. In this analysis, v_1 is computed using event-plane method in which we estimate the reaction plane, called the event plane, from the observed event plane angle determined from the anisotropic flow. The formula used for v_1 calculations is:

$$v_1 = \langle \cos(\phi - \Psi) \rangle \quad (1-5)$$

Where Ψ represents the azimuth angle of the event plane reconstructed using ZDC detector, ϕ is the reaction plane angle of outgoing particles and R_Ψ is the event plane resolution. The inner brackets $\langle \dots \rangle$ denote the average of tracks within a single event, and the outer brackets indicate the average across all events. Finally, the v_1 measured using equation 1.5 is divided by event plane resolution to obtain resolution corrected directed flow (v_1).

$$v_1 = \frac{\langle \cos(\phi - \Psi) \rangle}{R_1} \quad (1-6)$$

Where, R_1 is the first order event plane resolution and this step is implemented for all the 9 centrality ranges.

1.6 Charge-dependent directed flow in U+U collisions at $\sqrt{s_{NN}} = 193$ GeV

In this section, we shall present the directed flow results of the three identified charged particles (π^\pm , K^\pm and $p(\bar{p})$). The v_1 dependence on rapidity, centrality and transverse momentum will be discussed for each particle species separately. For all the particles/antiparticles, v_1 is calculated by taking the average of $\cos(\phi - \Psi)$ and then divided it by the event plane resolution as discussed in the previous section.

1.6.1 Directed flow of π^\pm meson

This section will present directed flow results of positive and negative charged pions. Fig.1.5 shows the directed flow of π^+ and π^- as a function of rapidity ($-0.8 < y < 0.8$) in U+U collisions at $\sqrt{s_{NN}} = 193$ GeV. No splitting is observed between π^+ and π^- in all the 9 centrality bins. Figure 1.6 shows $a_1 = \langle \sin(\phi - \Psi) \rangle$ as a function of rapidity (measured to check the detector performance). The observed zero a_1 shows that the detectors are working properly. Figure 1.7 shows the slope (dv_1/dy) for π^+ and π^- as a function of centrality. A negative slope with increase in v_1 magnitude from central to peripheral collisions is observed for both π^+ and π^- . The Δv_1 and Δa_1 slopes are presented in figure 1.8. The Δv_1 of pion is consistent with zero (within uncertainties) for all the centrality bins except 60-70% where it is almost 2σ above the zero line. The Δa_1 slope is plotted as a bench mark to see the residual detector effects in the corrected event plane. The Δa_1 is found smaller than zero in both mid-central and central collisions. v_1 and Δv_1 as a function of p_T for π^+ and π^- is shown in figures 1.9 and 1.10 respectively. No significant splitting is observed between π^+ and π^- with respect to p_T as well and it is true for both mid-central (10-40%) and peripheral (40-80%) collisions. The mid central results shows that v_1 changes sign at higher $p_T > 1.4$ GeV/c for π^+ , while it remains negative in the peripheral collisions for both positive and negative pions. The $\Delta v_1(p_T)$ is also found consistent with zero at low p_T range with a sign change for mid-central result at higher $p_T > 1.5$ GeV/c.

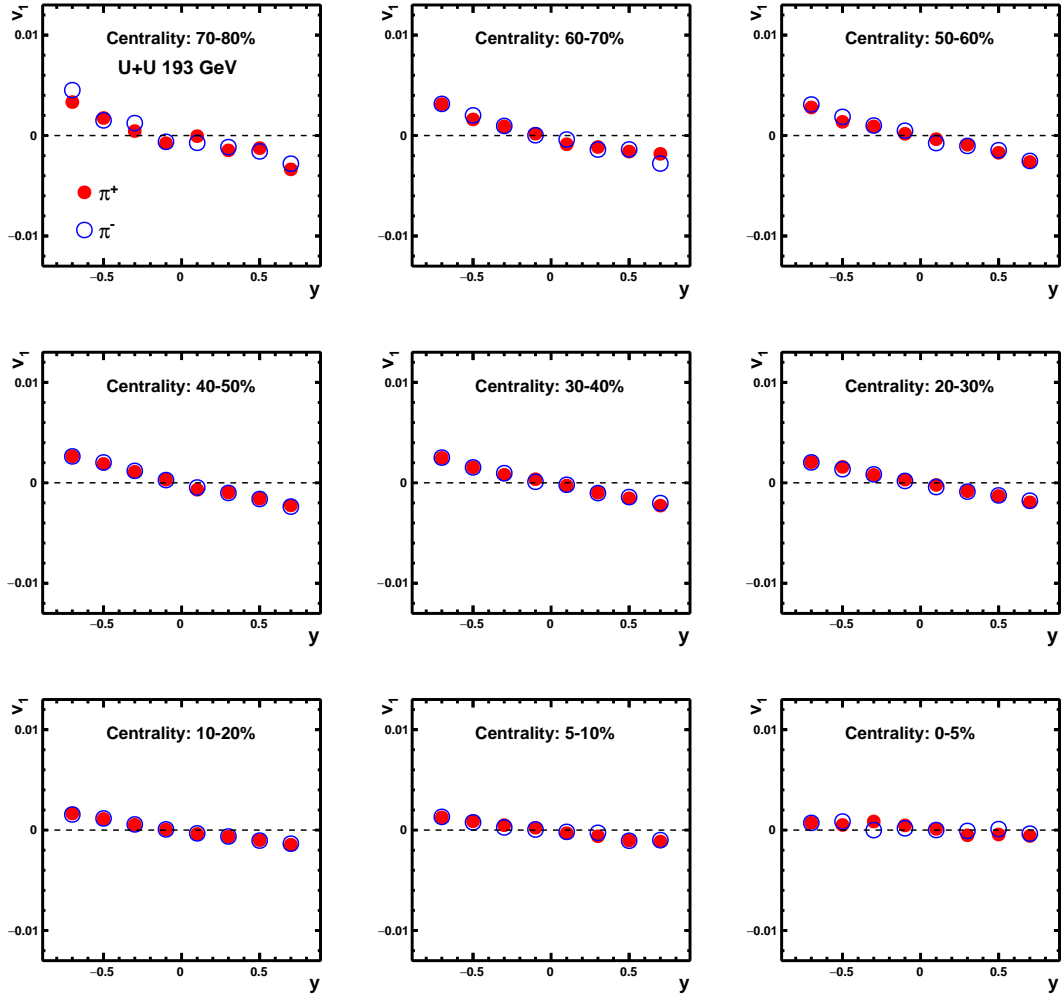


Figure 1-5 Directed flow of π^+ (red solid circles) and π^- (blue open circles) as a function of rapidity at 193 GeV U+U collisions. From top left to bottom right, centrality changes from peripheral to central.

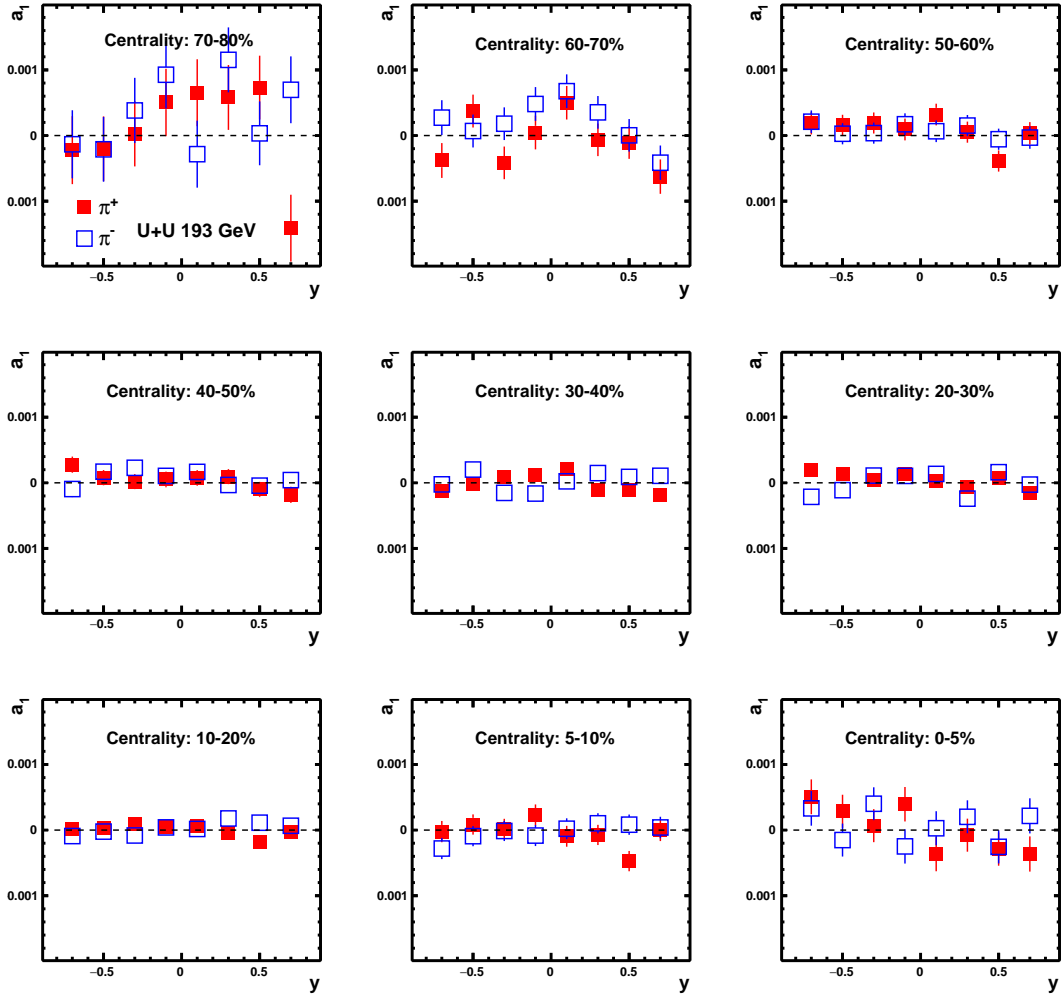


Figure 1-6 $a_1 = \langle \sin(\phi - \Psi) \rangle$ of π^+ (red solid squares) and π^- (blue open squares) as a function of rapidity at 193 GeV U+U collisions. From top left to bottom right, centrality changes from peripheral to central.

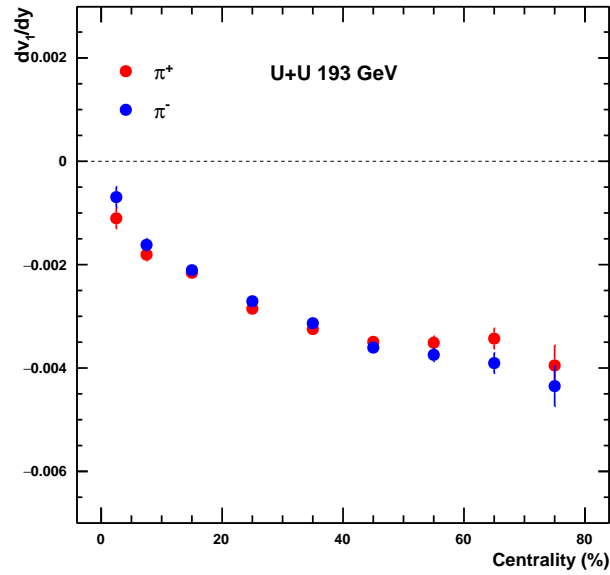


Figure 1-7 The slope (dv_1/dy) of π^+ (red solid circles) and π^- (blue solid circles) as a function of centrality at 193 GeV U+U collisions.

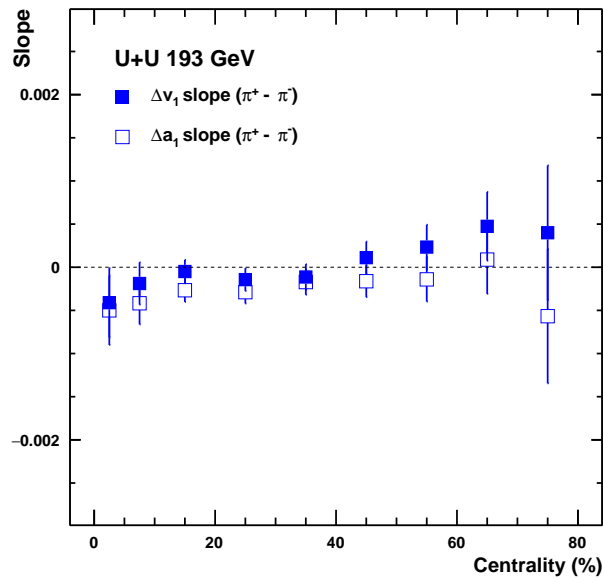


Figure 1-8 The Δv_1 and Δa_1 slopes between π^+ and π^- as a function of centrality at 193 GeV U+U collisions. The Δa_1 slope is shown as benchmark.

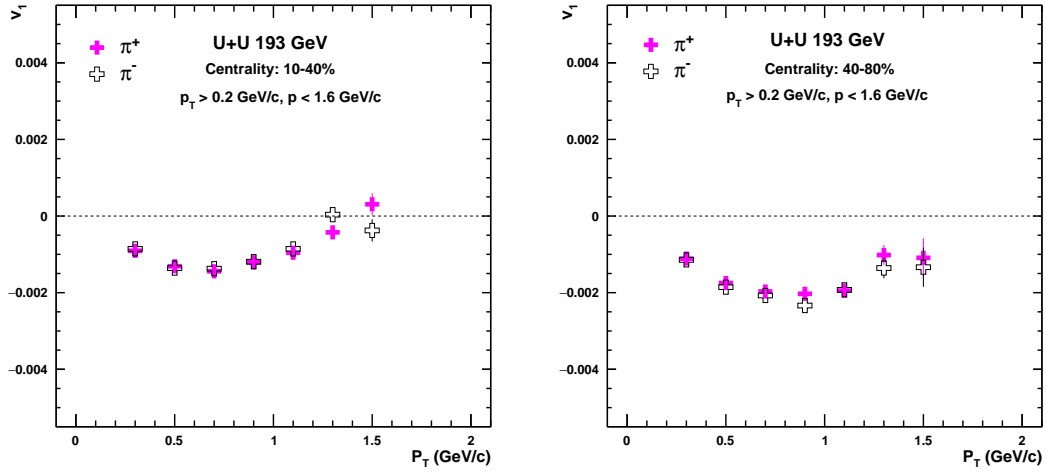


Figure 1-9 v_1 as a function of p_T between π^+ and π^- at 193 GeV U+U collisions. The solid pink marker represents π^+ and the open black marker stands for π^- .

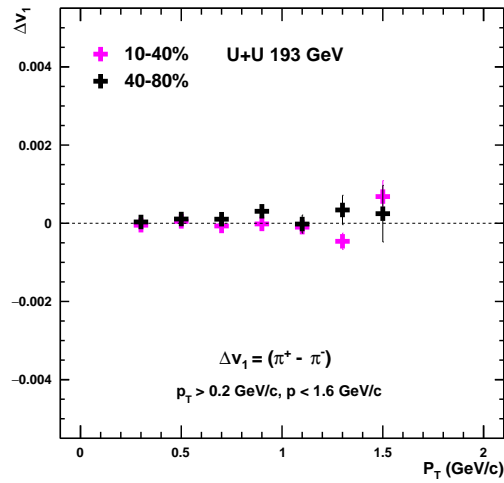


Figure 1-10 The Δv_1 as a function of p_T for pion at 193 GeV U+U collisions. The pink marker is used for 10-40% centrality and the black marker represents 40-80% centrality

1.6.2 Directed flow of K^\pm meson

In this section, we shall present directed flow results of positive and negative kaons in U+U collisions at $\sqrt{s_{NN}} = 193$ GeV. Fig. 1.11 represents v_1 of K^+ and K^- as a function of rapidity ($-0.8 < y < 0.8$). No significant splitting is observed between positive and negative kaons, similar to pions. Figure 1.12 shows the $a_1 = \langle \sin(\phi - \Psi) \rangle$ as a function of rapidity (shown as a benchmark) and is consistent with zero for all the centralities. Figure 1.13 shows (dv_1/dy) slope of K^+ and K^- as a function of centrality. A considerable splitting between the slopes of positive and negative charged kaons is observed in the mid-central (10-40%) collisions. Figure 1.14 shows centrality dependent Δv_1 and Δa_1 slopes. The Δv_1 slope shows a decreasing trend from mid-central to peripheral collisions, whereas Δa_1 slope is found consistent with zero. Moreover, the negative Δv_1 slope for kaons (in the peripheral) can serve as a possible clue of electromagnetic effect. Figure 1.15 shows v_1 as a function of p_T between K^+ and K^- in the mid-central (10-40%) and peripheral (40-80%) collisions. The mid-central results show a significant splitting of $v_1(p_T)$ between positive and negative kaons at a transverse momentum range ($0.5 < p_T < 1.3$) GeV/c. In contrast, no splitting is observed between K^+ and K^- for peripheral collisions. Figure 1.16 shows Δv_1 dependence on p_T . The $\Delta v_1(p_T)$ increases from lower p_T range to higher p_T range upto 1.3 GeV/c in the mid central collisions, whereas no obvious (p_T) dependence is observed for peripheral collisions within uncertainties.

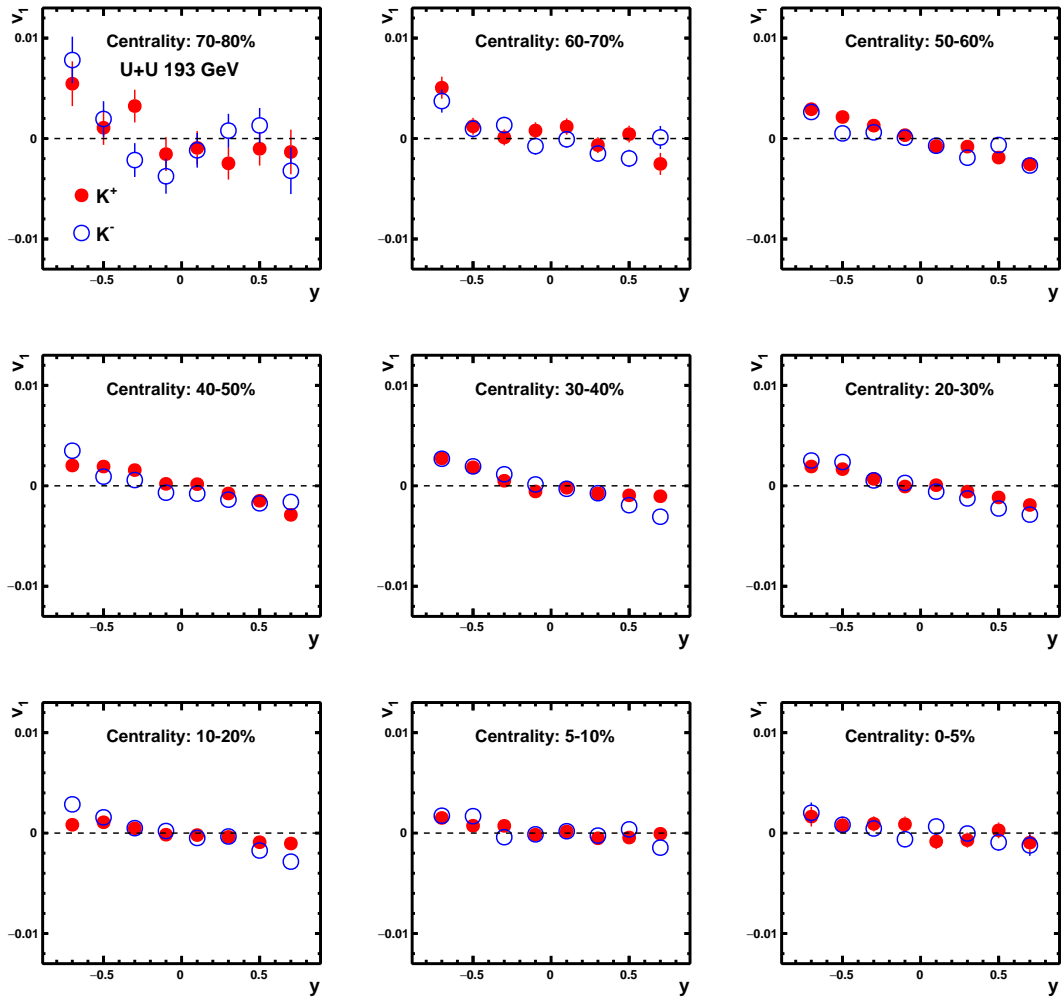


Figure 1-11 Directed flow of K^+ (red solid circles) and K^- (blue open circles) as a function of rapidity at 193 GeV U+U collisions. From top left to bottom right, centrality changes from peripheral to central.

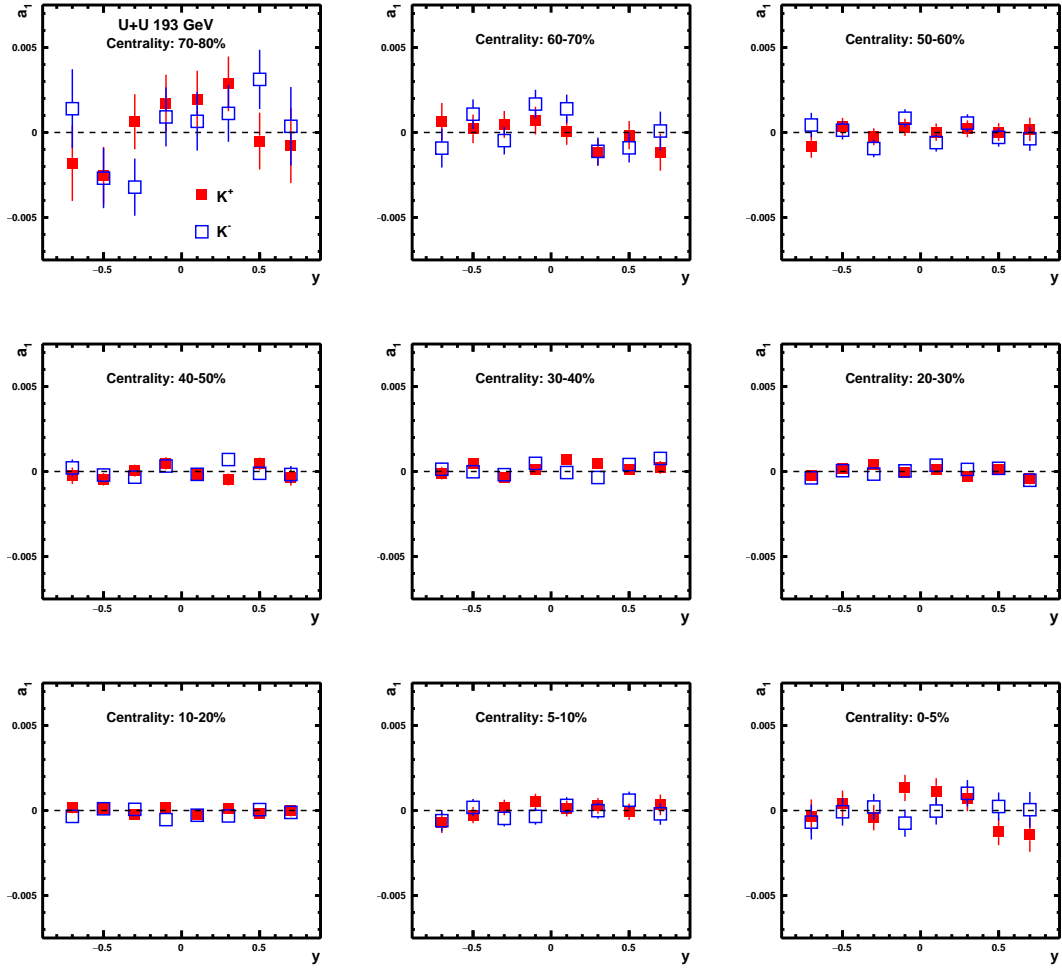


Figure 1-12 $a_1 = \langle \sin(\phi - \Psi) \rangle$ of K^+ (red solid circles) and K^- (blue open circles) as a function of rapidity at 193 GeV U+U collisions. From top left to bottom right, centrality changes from peripheral to central.

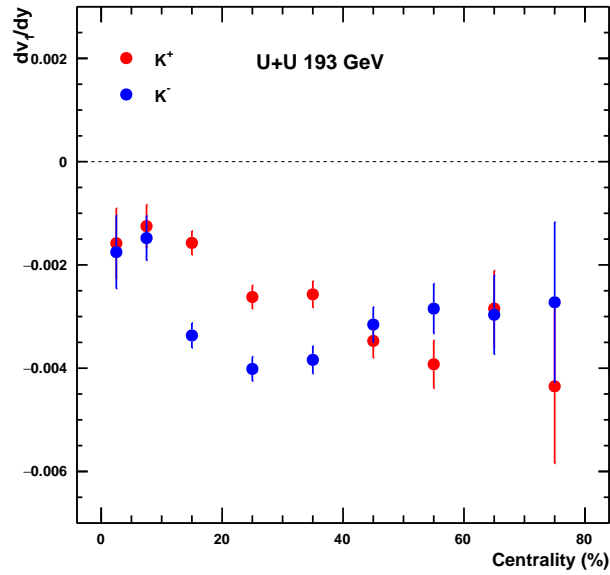


Figure 1-13 The slope (dv_1/dy) of K^+ (red solid circles) and K^- (blue solid circles) as a function of rapidity at 193 GeV U+U collisions.

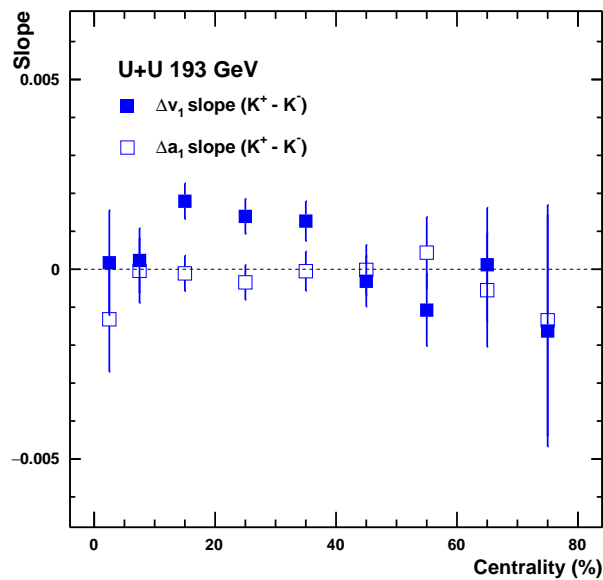


Figure 1-14 The Δv_1 and Δa_1 slopes between K^+ and K^- as a function of centrality at 193 GeV U+U collisions. The Δa_1 slope is shown as benchmark.

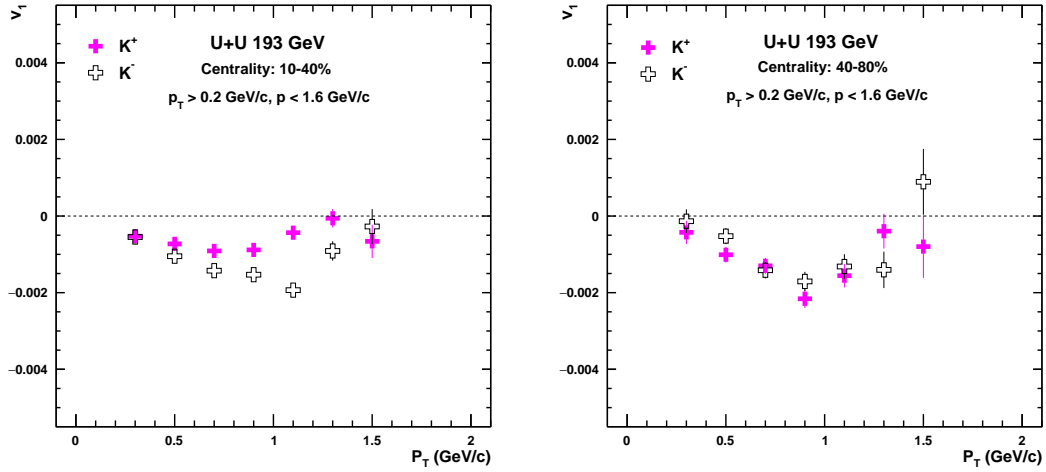


Figure 1-15 v_1 as a function of p_T between K^+ and K^- at 193 GeV U+U collisions. The solid pink marker represents K^+ and the open black marker stands for K^- .

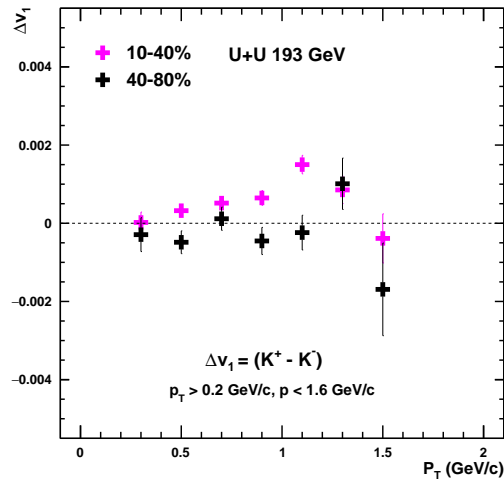


Figure 1-16 The Δv_1 as a function of p_T for kaon at 193 GeV U+U collisions. The pink marker is used for 10-40% centrality and the black marker represents 40-80% centrality

1.6.3 Directed flow of p and \bar{p}

The directed flow of proton and antiproton in U+U collisions at $\sqrt{s_{NN}} = 193$ GeV will be presented in this section. Fig.1.17 shows v_1 dependence on rapidity ($-0.8 < y < 0.8$) for all the 9 centralities. A significant splitting between p and \bar{p} is observed in the mid-central collisions (10-40%). Figure 1.18 is the $a_1 = \langle \sin(\phi - \Psi) \rangle$ measurement which is shown as benchmark. The slopes (dv_1/dy) between p and \bar{p} as well as Δv_1 and Δa_1 are presented in figure 1.19 and 1.20 respectively. The Δv_1 shows a decreasing trend, with positive in the central collisions and negative in the peripheral, whereas Δa_1 slope is found consistent with zero line. Figure 1.21 shows v_1 as a function of p_T between p and \bar{p} in 10-40% and 40-80% centralities. For mid-central (10-40%) results, the splitting between proton and anti-proton increases as we move from lower p_T range to higher p_T range upto 1.5 GeV/c. For proton, v_1 also changes sign in the mid-central collisions at p_T range (> 1.2 GeV/c). In contrast, no splitting is observed between p and \bar{p} in the peripheral collisions, and the v_1 magnitude remains negative in all the p_T bins. The $\Delta v_1(p_T)$ in figure 1.22 also shows a similar increasing trend from lower p_T to higher p_T upto 1.5 GeV/c for mid central results, whereas for peripheral, no clear p_T dependence is shown in figure 1.22.

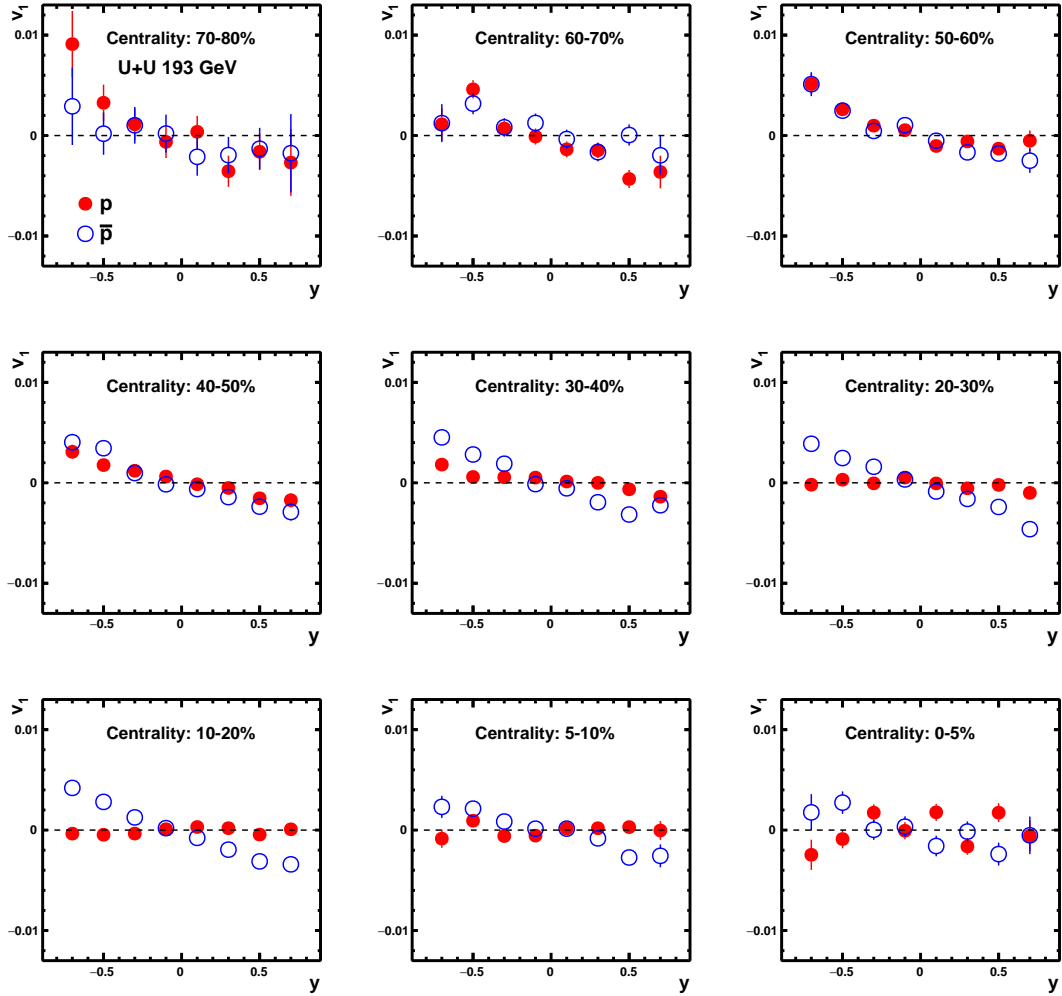


Figure 1-17 Directed flow of p (red solid circles) and \bar{p} (blue open circles) as a function of rapidity at 193 GeV U+U collisions. From top left to bottom right, centrality changes from peripheral to central.

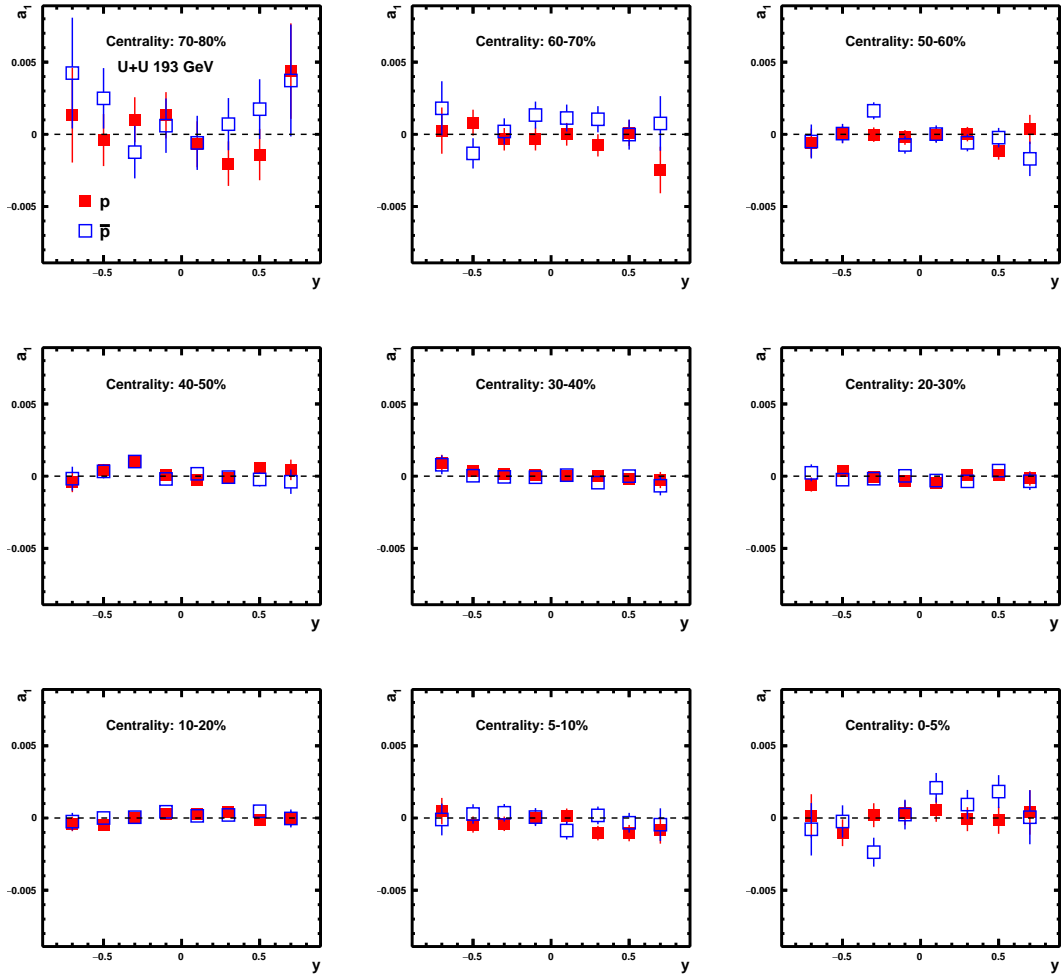


Figure 1-18 $a_1 = \langle \sin(\phi - \Psi) \rangle$ of p (red solid circles) and \bar{p} (blue open circles) as a function of rapidity at 193 GeV U+U collisions. From top left to bottom right, centrality changes from peripheral to central.

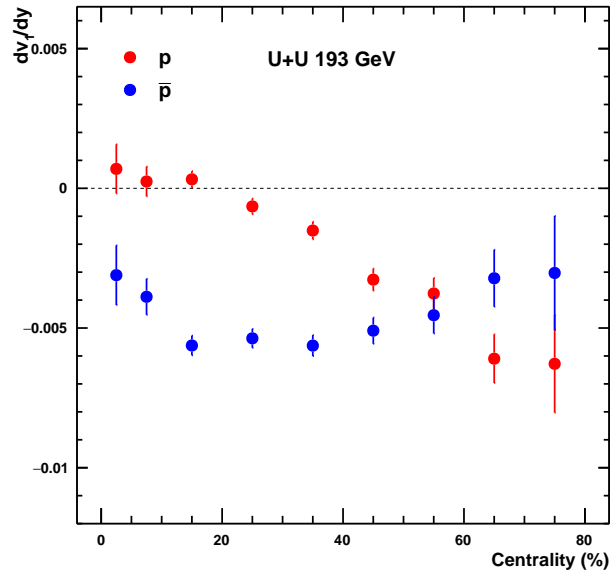


Figure 1-19 The slope (dv_1/dy) of p (red solid circle) and \bar{p} (blue solid circles) as a function of centrality at 193 GeV U+U collisions.

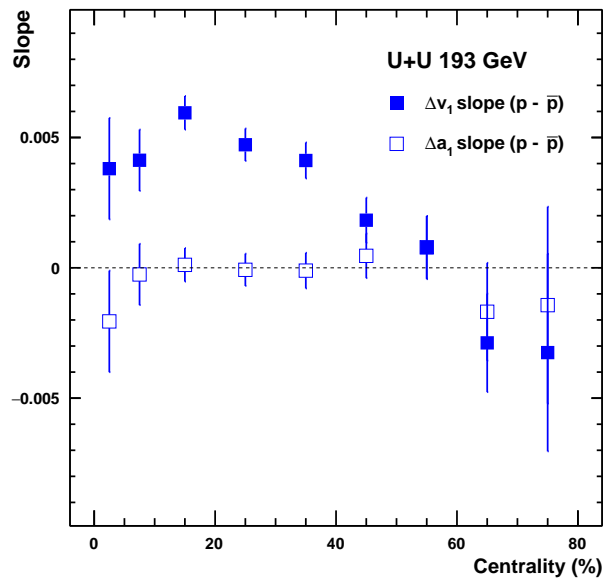


Figure 1-20 The Δv_1 and Δa_1 slopes between p and \bar{p} as a function of centrality at 193 GeV U+U collisions. The Δa_1 slope is shown as benchmark.

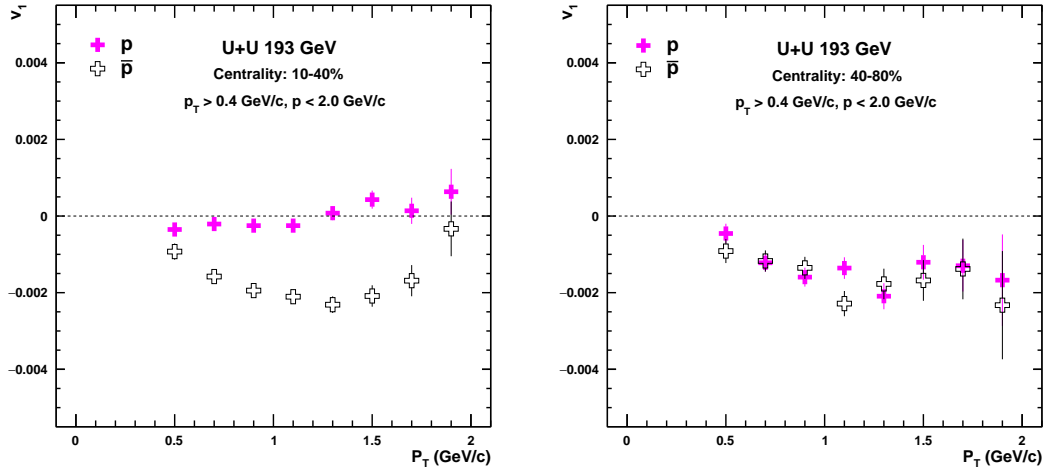


Figure 1-21 v_1 as a function of p_T between p and \bar{p} at 193 GeV U+U collisions. The solid pink marker represents p and the open black marker stands for \bar{p} .

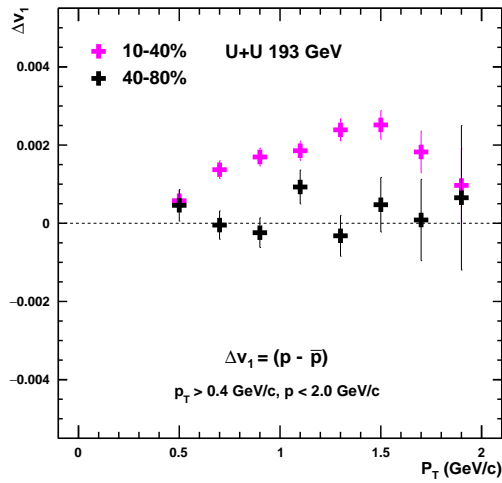


Figure 1-22 The Δv_1 as a function of p_T for proton at 193 GeV U+U collisions. The pink marker is used for 10-40% centrality and the black marker represents 40-80% centrality

1.7 Systematic Uncertainties Evaluation

The systematic uncertainties are evaluated by varying event, track and PID selection criteria. For all the systematic checks, we only vary one cut at a time and keep all others as default. Beside the variations in event and track cuts, we also consider the difference between forward and backward rapidity as a source of systematic uncertainty in this analysis. The default values of various event and track cuts as well as the varied values for systematic uncertainty measurements are summarized in table 1.3.

Table 1-3 The sources of systematic uncertainties in U+U collisions at $\sqrt{s_{NN}} = 193$ GeV

Default	Systematic
$-50 < V_z^{\text{TPC}} < 50$ cm	$-50 < V_z^{\text{TPC}} < 0$ cm
$N_{fits} > 15$	$N_{fits} > 20$
$-0.8 < y < 0.8$	$-0.8 < y < 0$
$-0.8 < y < 0.8$	$0 < y < 0.8$
DCA < 3 cm	DCA < 1 cm
DCA < 3 cm	DCA < 1.5 cm
$-2.0 < n\sigma^{\text{TPC}} < 2.0$	$-1.0 < n\sigma^{\text{TPC}} < 1.0$
$-2.0 < n\sigma^{\text{TPC}} < 2.0$	$-1.5 < n\sigma^{\text{TPC}} < 1.5$
$m^2(\text{pi}) = -0.01 - 0.10$ (GeV/c ²) ²	$m^2(\text{pi}) = -0.009 - 0.09$ (GeV/c ²) ²
$m^2(\text{k}) = 0.20 - 0.35$ (GeV/c ²) ²	$m^2(\text{k}) = 0.21 - 0.34$ (GeV/c ²) ²
$m^2(\text{p}) = 0.80 - 1.0$ (GeV/c ²) ²	$m^2(\text{p}) = 0.82 - 0.98$ (GeV/c ²) ²
$m^2(\text{p}) = 0.80 - 1.0$ (GeV/c ²) ²	$m^2(\text{p}) = 0.84 - 0.96$ (GeV/c ²) ²

The Barlow test method is used to calculate all the systematic uncertainties caused by statistical fluctuations. The standard formula for Barlow test can be written as:

$$\sigma_i = \frac{\sqrt{(Y_i - Y_d)^2 - |eY_i^2 - eY_d^2|}}{\sqrt{12}} \quad (1-7)$$

$$\sigma = \sqrt{\sum \sigma_i^2} \quad (1-8)$$

Where Y_i is the variation, Y_d is the default value and eY_i as well as eY_d are the statistical errors in the varied and default values respectively. The final result of sys-

tematic uncertainty is represented by σ . However, in most cases, the statistical error is too large causing the magnitude of systematic uncertainty smaller than statistical uncertainty. In this analysis, we have used a modified form of Barlow test in which the term $|eY_i^2 - eY_d^2|$ is eliminated from the standard Barlow test method. This actual formula used for systematic uncertainty calculations is written as:

$$\sigma_i = \frac{|Y_i - Y_d|}{\sqrt{12}} \quad (1-9)$$

$$\sigma = \sqrt{\sum \sigma_i^2} \quad (1-10)$$

Now, we shall present the systematic uncertainty results of directed flow for the three identified charged particles (π^\pm , K^\pm and $p(\bar{p})$) in U+U collisions at $\sqrt{s_{NN}} = 193$ GeV. Figures 1.23 to 1.34 show the variations of v_1 as a function of rapidity for different event and track cuts and the systematic uncertainties are calculated in both mid-central (10-40%) and peripheral (40-80%) collisions. The systematic variation in dv_1/dy and $\Delta(dv_1/dy)$ as a function of centrality are presented in figures 1.35 to 1.43. Whereas, the systematic results of v_1 with rest to p_T are shown in figures 1.44 to 1.55 respectively.

1.7.1 Systematic Uncertainty of v_1 as a function of rapidity

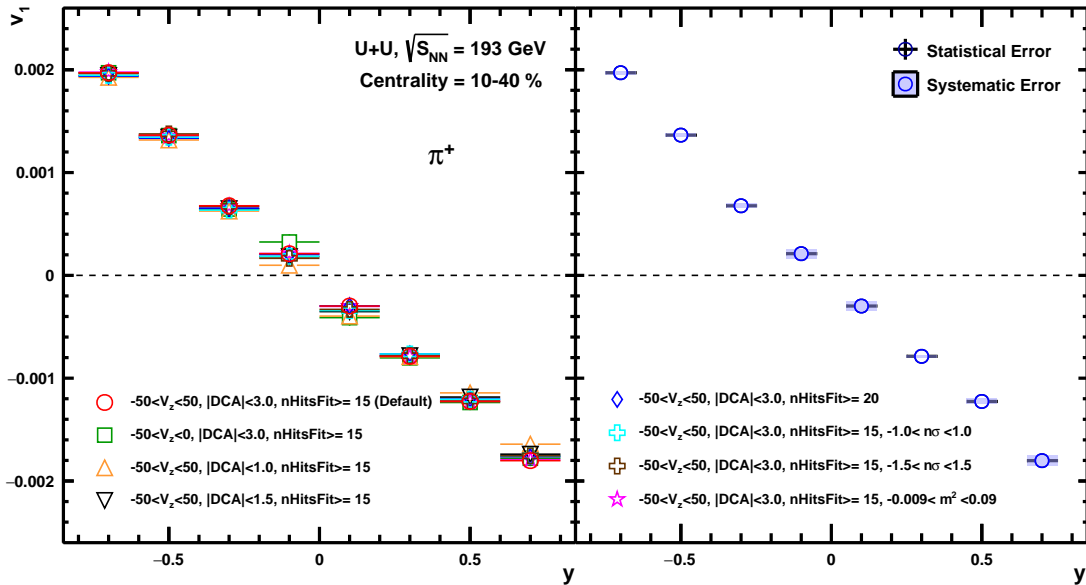


Figure 1-23 v_1 of π^+ for various systematic cuts (left panel) and the systematic/statistical error (right panel) in 10-40% centrality.

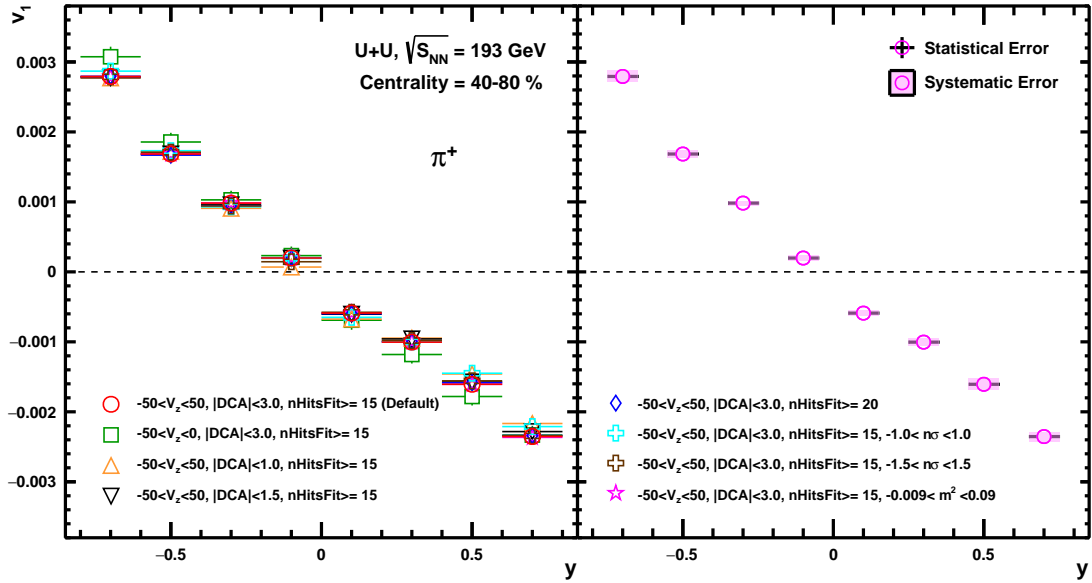


Figure 1-24 v_1 of π^+ for various systematic cuts (left panel) and the systematic/statistical error (right panel) in 40-80% centrality.

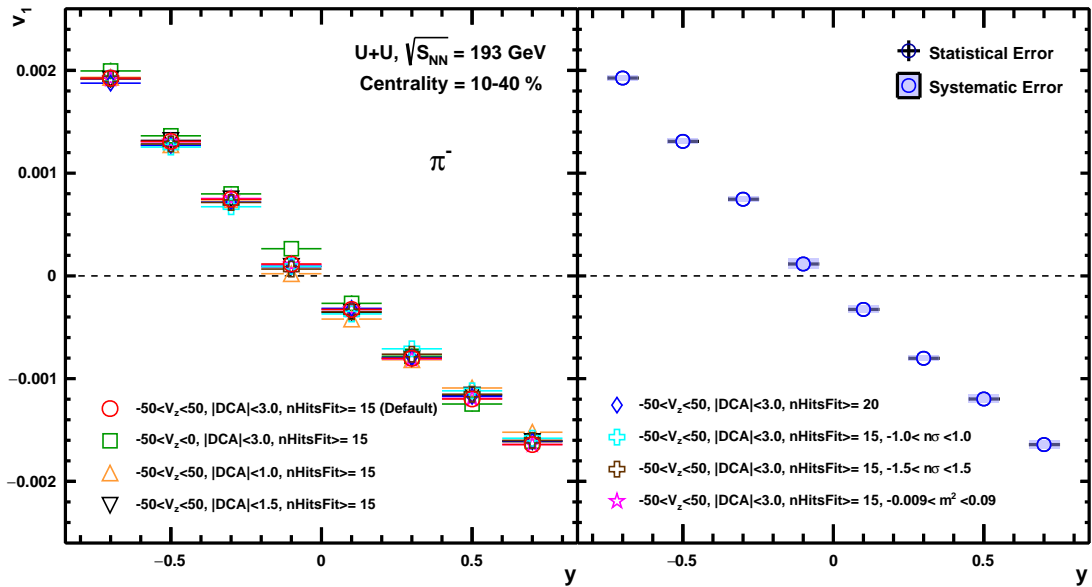


Figure 1-25 v_1 of π^- for various systematic cuts (left panel) and systematic/statistical error (right panel) in 10-40% centrality.

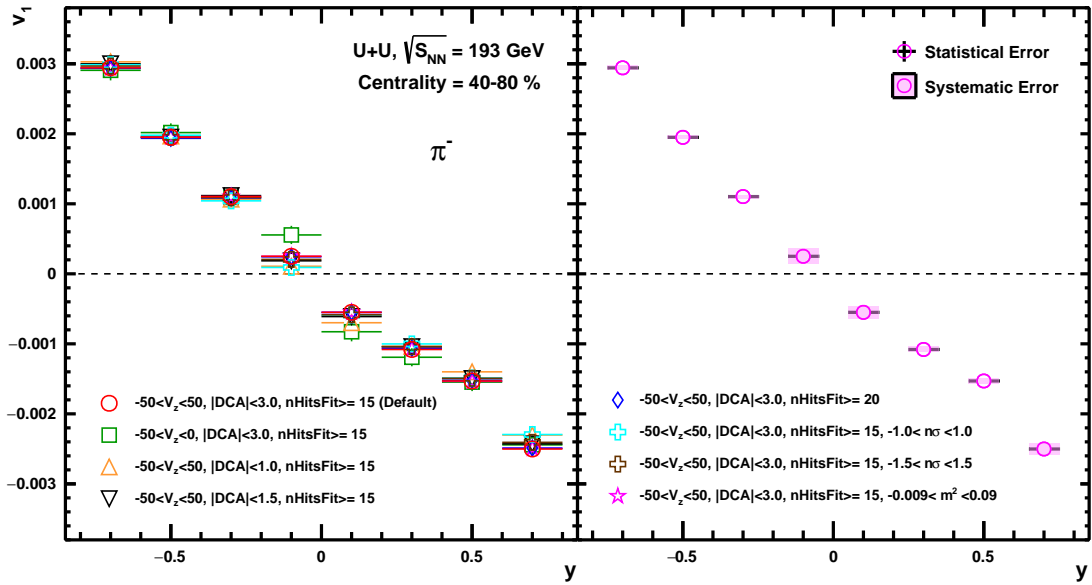


Figure 1-26 v_1 of π^- for various systematic cuts (left panel) and systematic/statistical error (right panel) in 40-80% centrality.

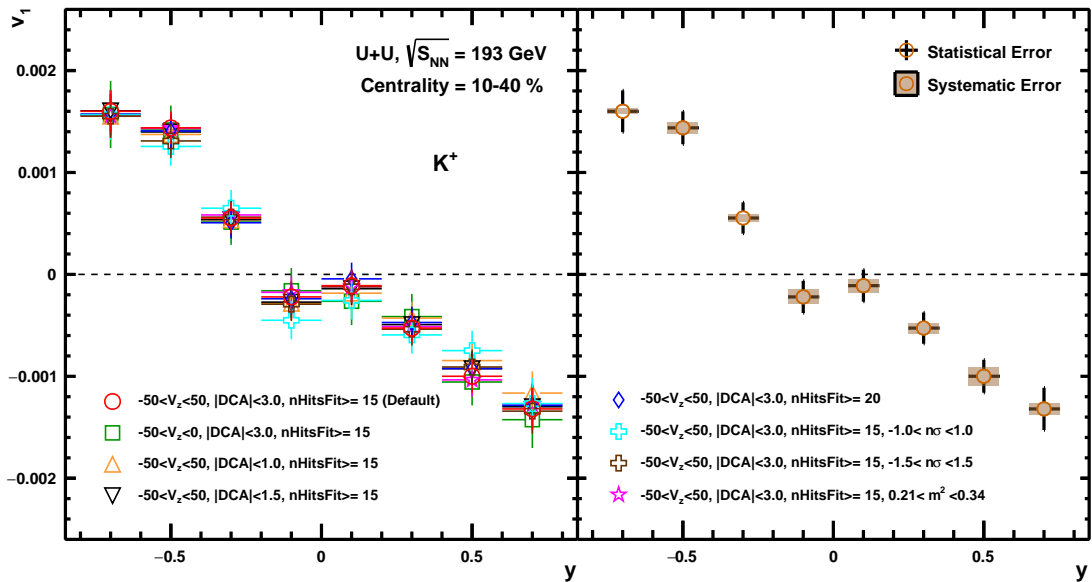


Figure 1-27 v_1 of K^+ for various systematic cuts (left panel) and the systematic/statistical error (right panel) in 10-40% centrality.

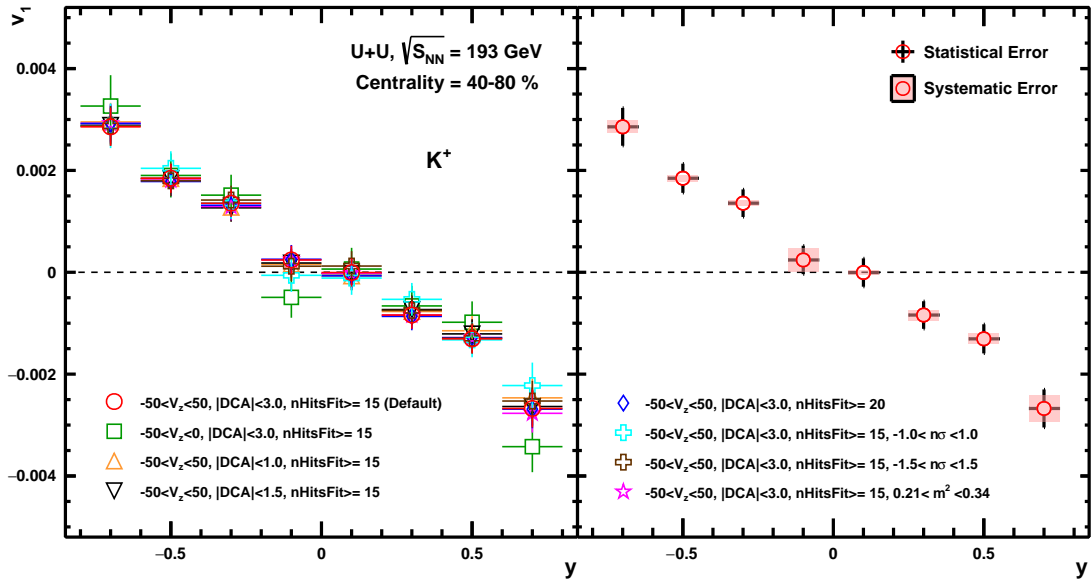


Figure 1-28 v_1 of K^+ for various systematic cuts (left panel) and the systematic/statistical error (right panel) in 40-80% centrality.

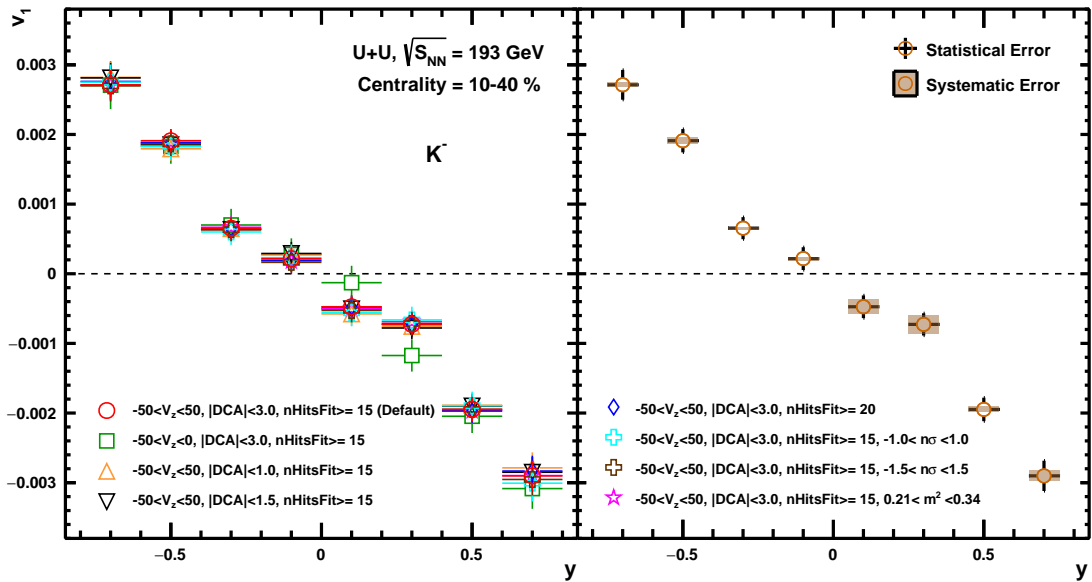


Figure 1-29 v_1 of K^- for various systematic cuts (left panel) and the systematic/statistical error (right panel) in 10-40% centrality.

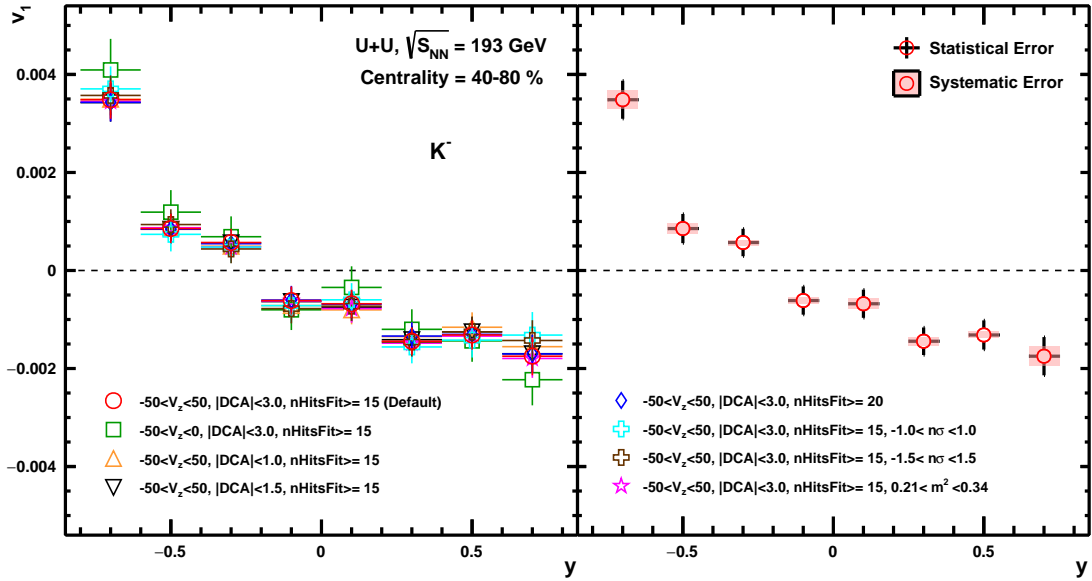


Figure 1-30 v_1 of K^- for various systematic cuts (left panel) and the systematic/statistical error (right panel) in 40-80% centrality.

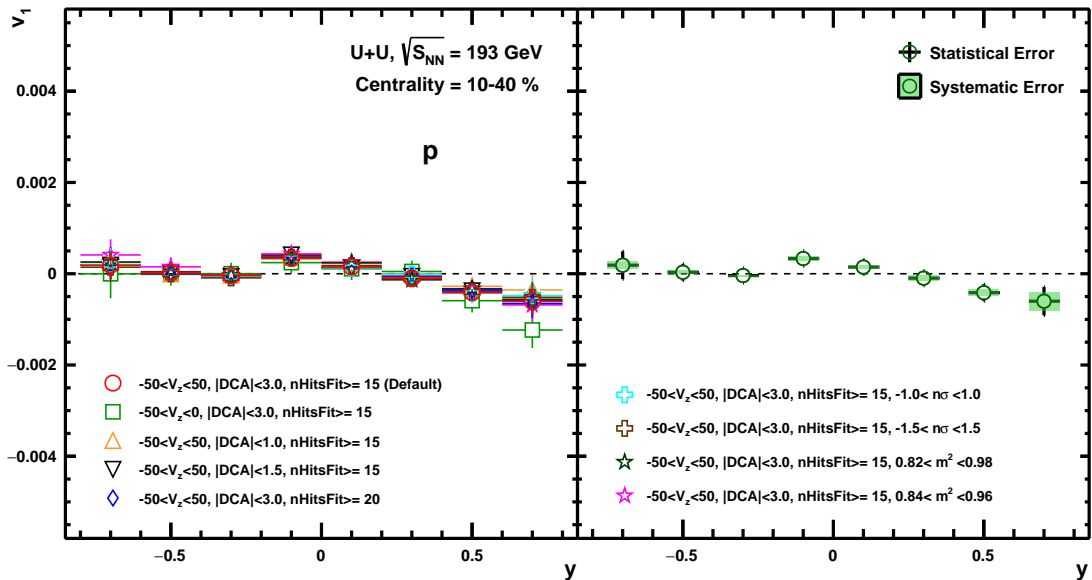


Figure 1-31 v_1 of p for various systematic cuts (left panel) and the systematic/statistical error (right panel) in 10-40% centrality.

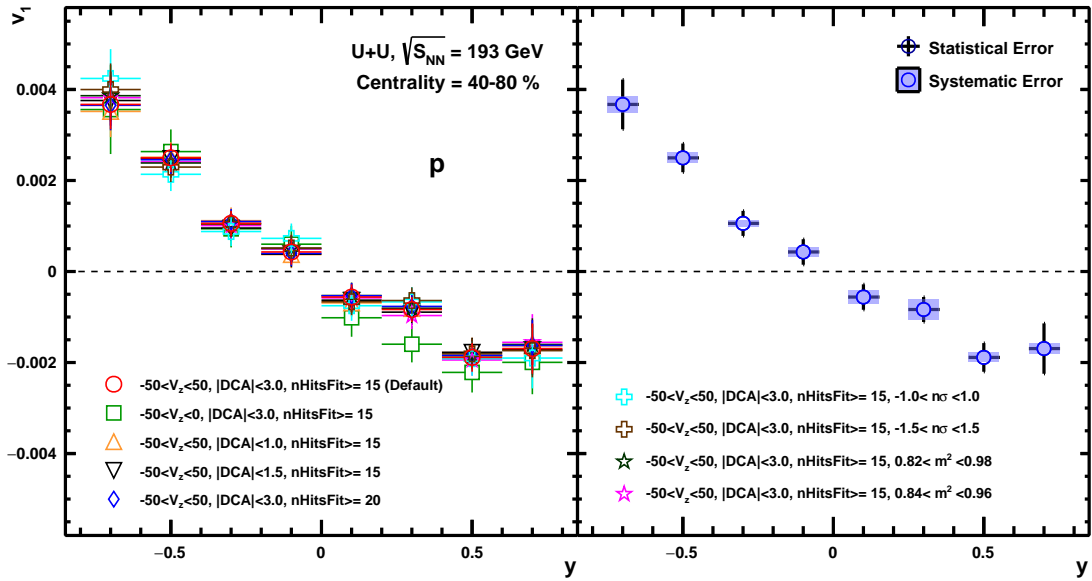


Figure 1-32 v_1 of p for various systematic cuts (left panel) and the systematic/statistical error (right panel) in 40-80% centrality.

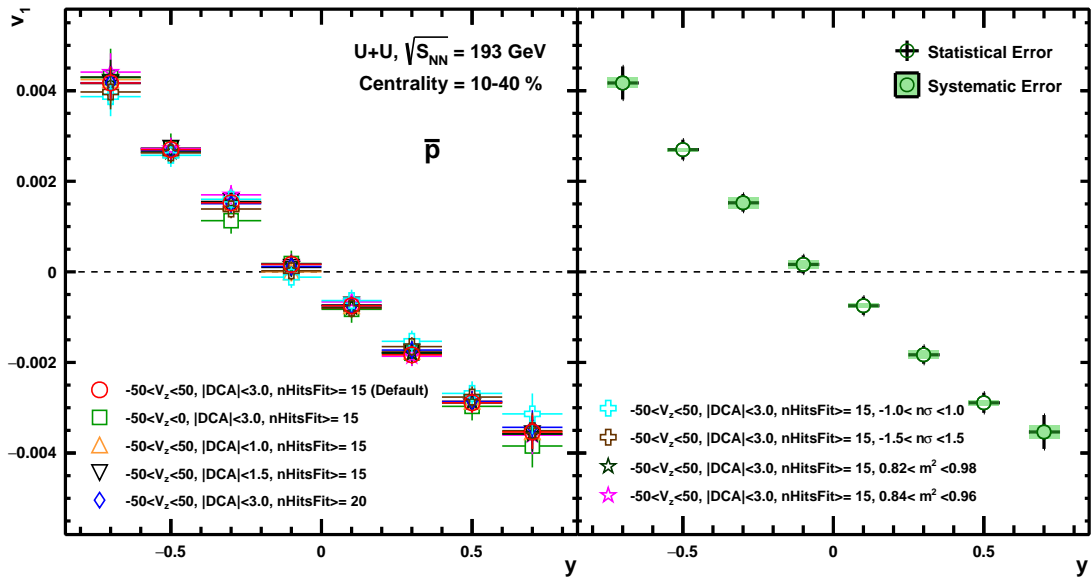


Figure 1-33 v_1 of \bar{p} for various systematic cuts (left panel) and the systematic/statistical error (right panel) in 10-40% centrality.

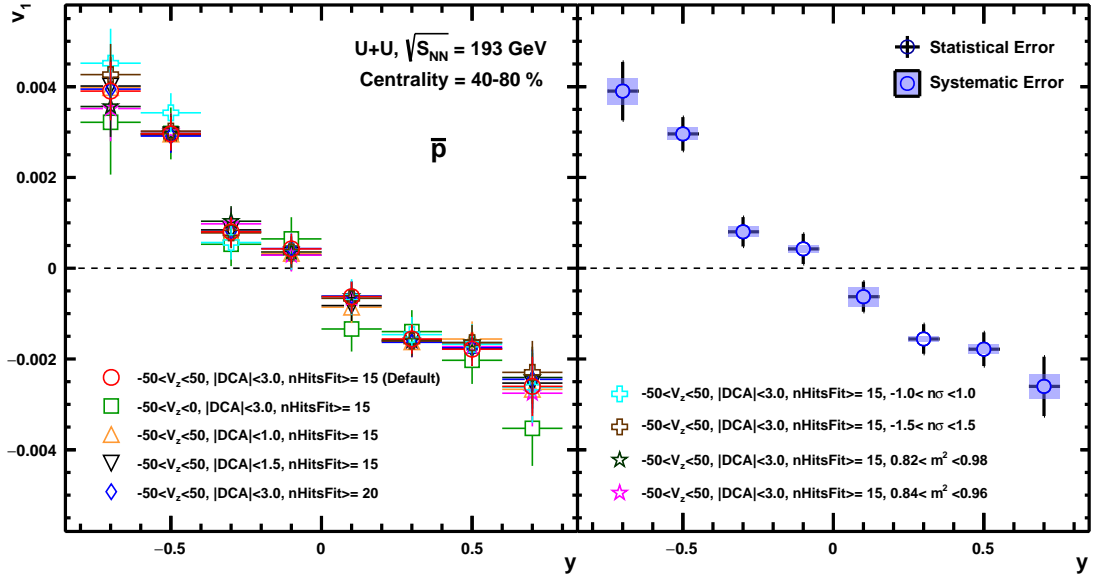


Figure 1-34 v_1 of \bar{p} for various systematic cuts (left panel) and the systematic/statistical error (right panel) in 40-80% centrality.

1.7.2 Systematic Uncertainty of dv_1/dy as a function of centrality

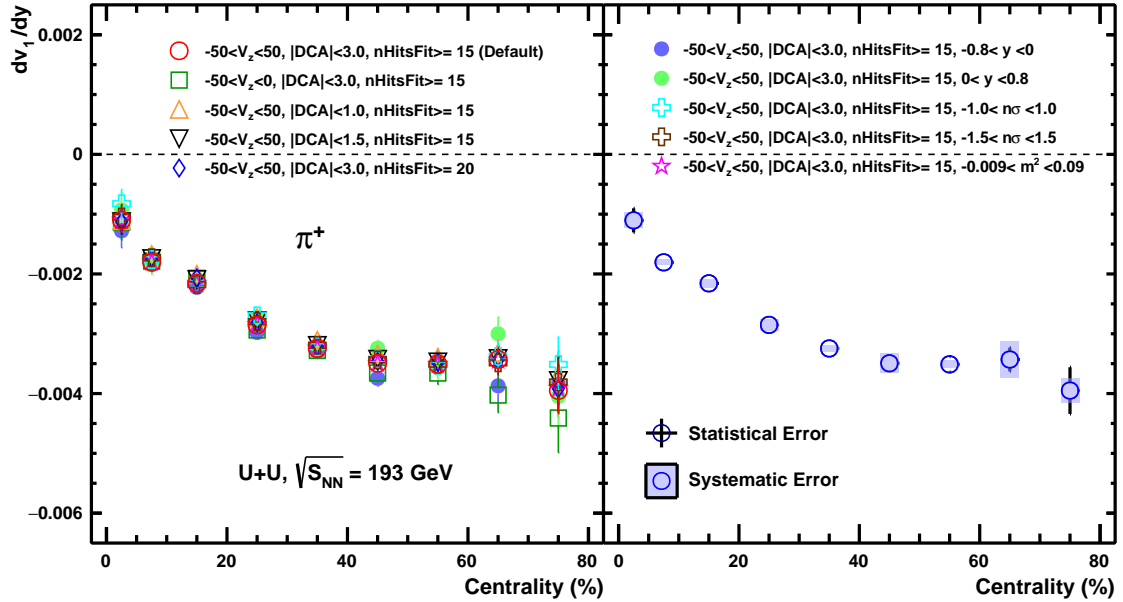


Figure 1-35 The slope (dv_1/dy) of π^+ for various systematic cuts (left panel) and the systematic/statistical error (right panel).

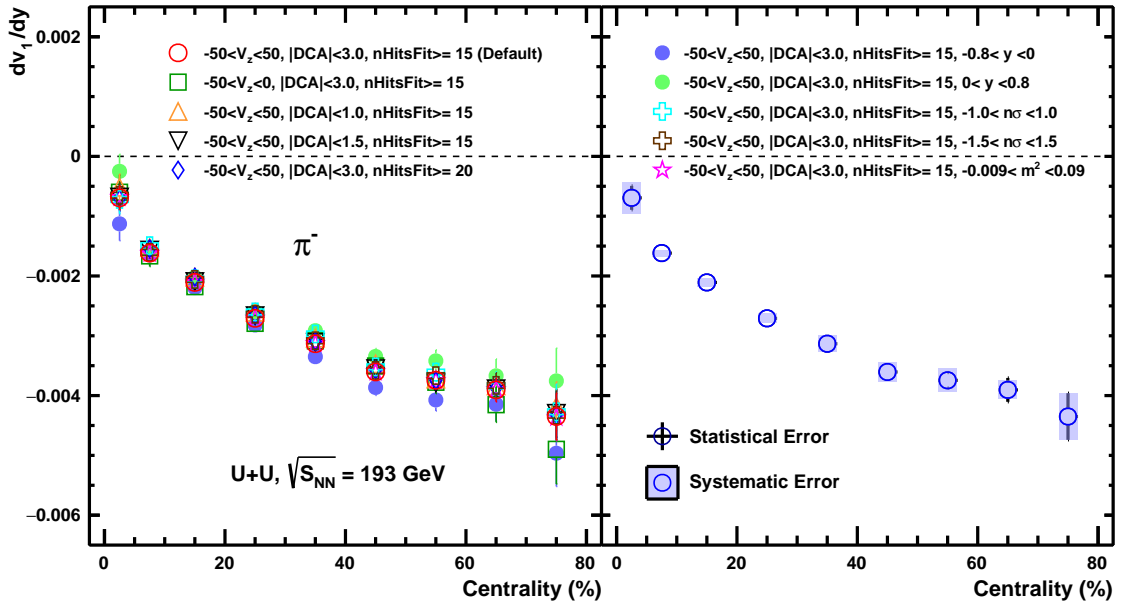


Figure 1-36 The slope (dv_1/dy) of π^- for various systematic cuts (left panel) and the systematic/statistical error (right panel).

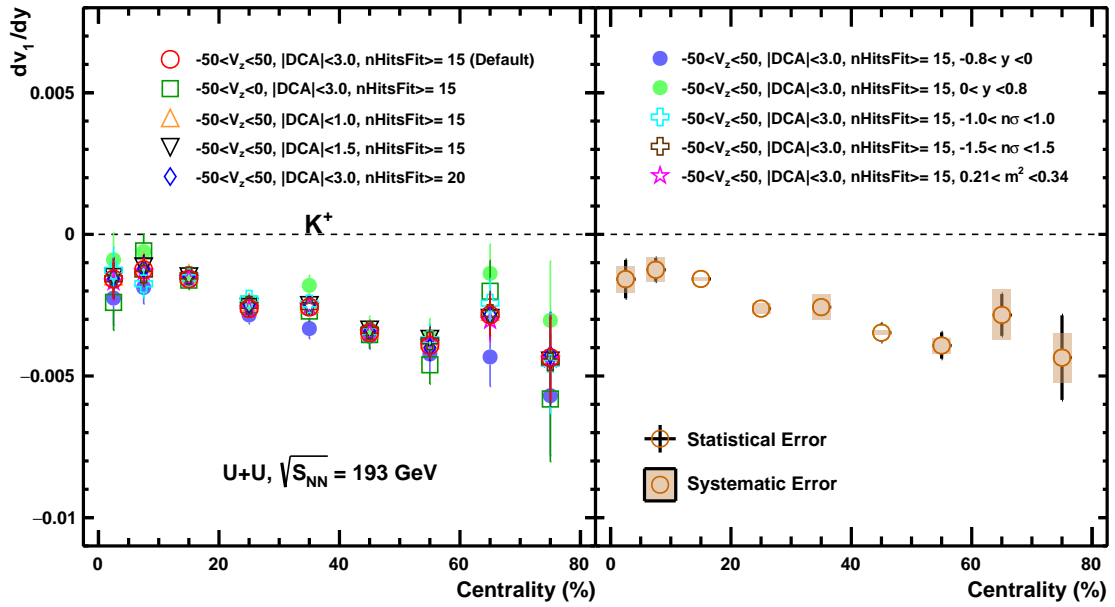


Figure 1-37 The slope (dv_1/dy) of K^+ for various systematic cuts (left panel) and the systematic/statistical error (right panel).

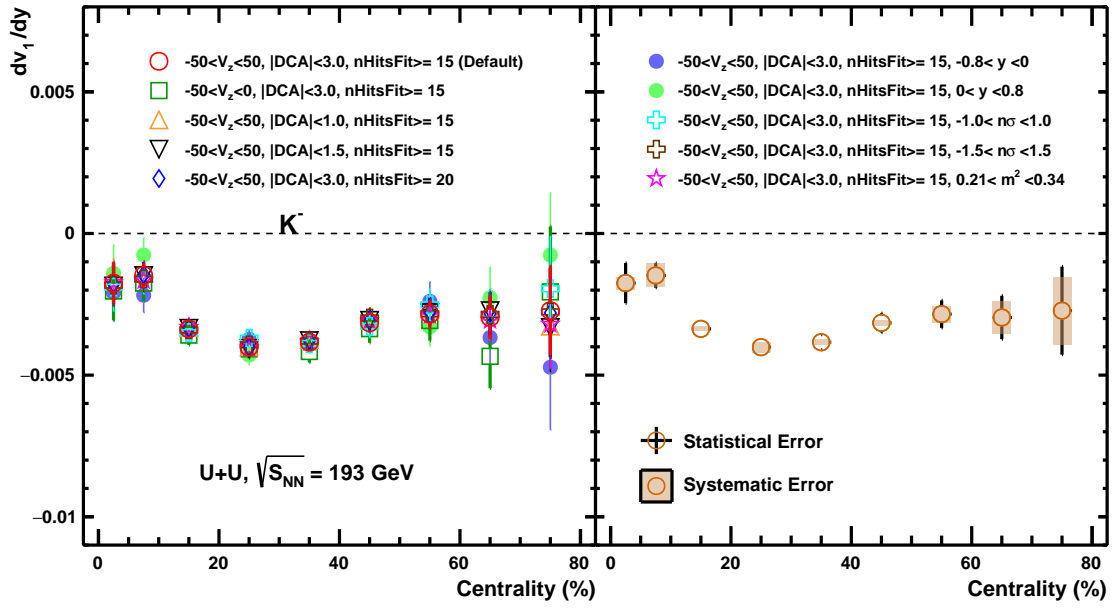


Figure 1-38 The slope (dv_1/dy) of K^- for various systematic cuts (left panel) and systematic/statistical error (right panel).

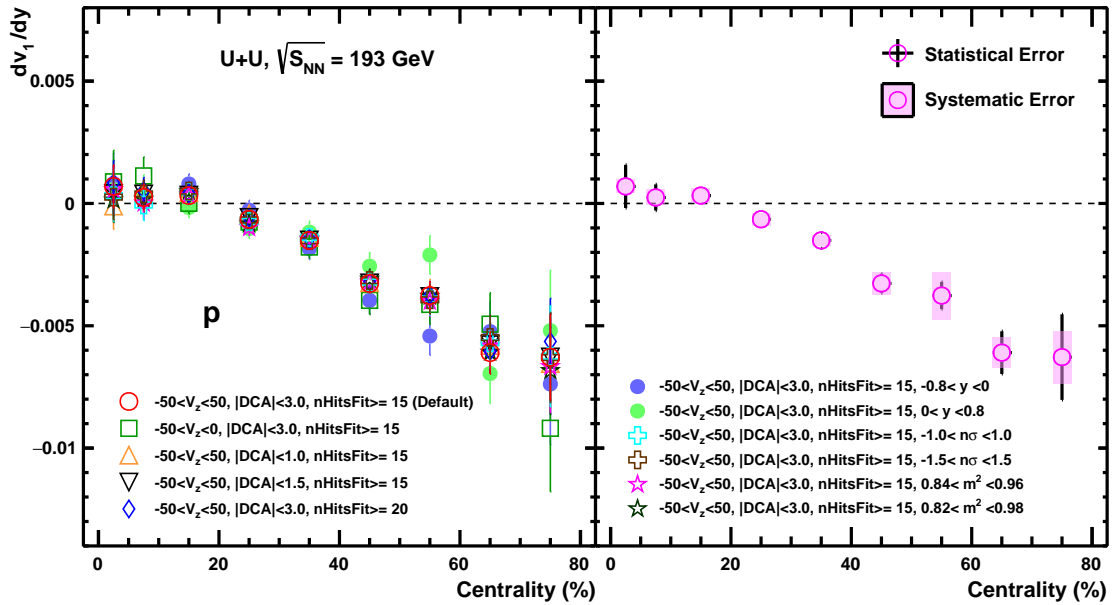


Figure 1-39 The slope (dv_1/dy) of p for various systematic cuts (left panel) and the systematic/statistical error (right panel)

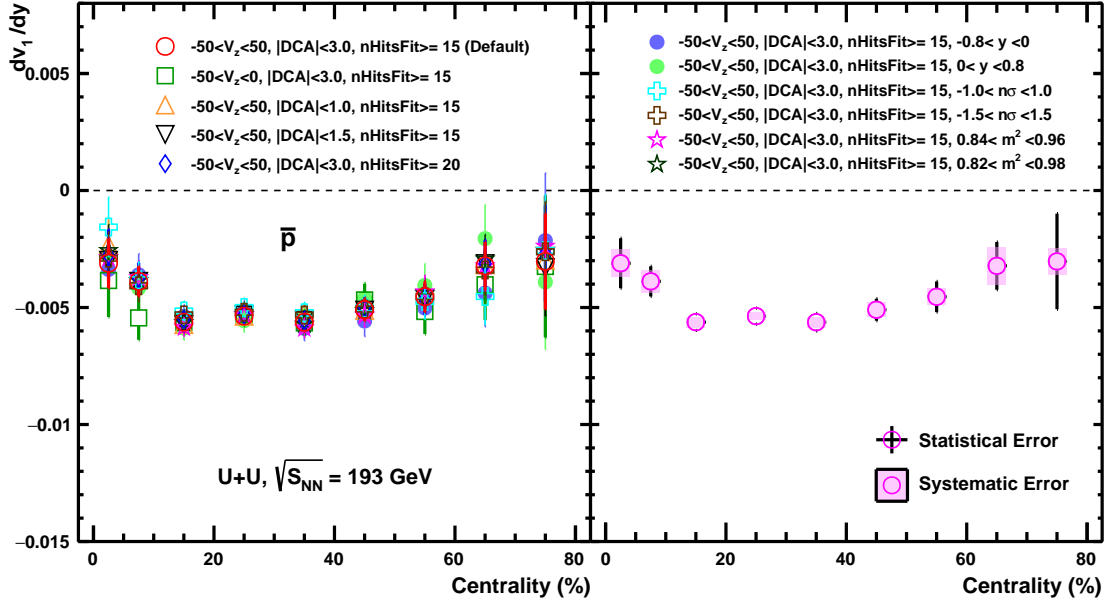


Figure 1-40 The slope (dv_1/dy) of \bar{p} for various systematic cuts (left panel) and the systematic/statistical error (right panel).

1.7.3 Systematic Uncertainty of $\Delta(dv_1/dy)$ as a function of centrality

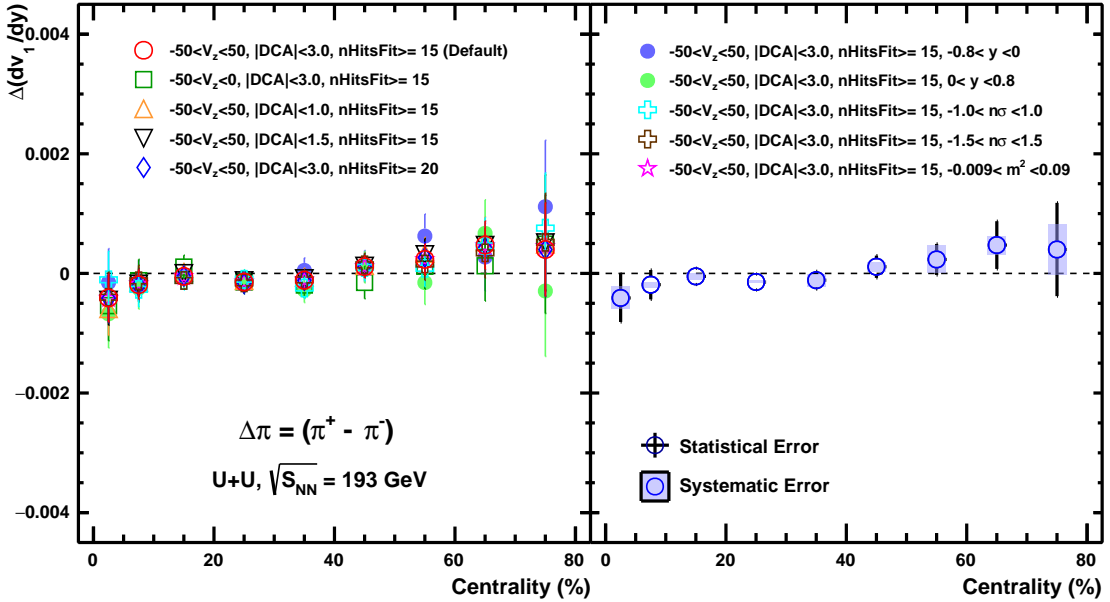


Figure 1-41 The $\Delta(dv_1/dy)$ of pion for various systematic cuts (left panel) and the systematic/statistical error (right panel).

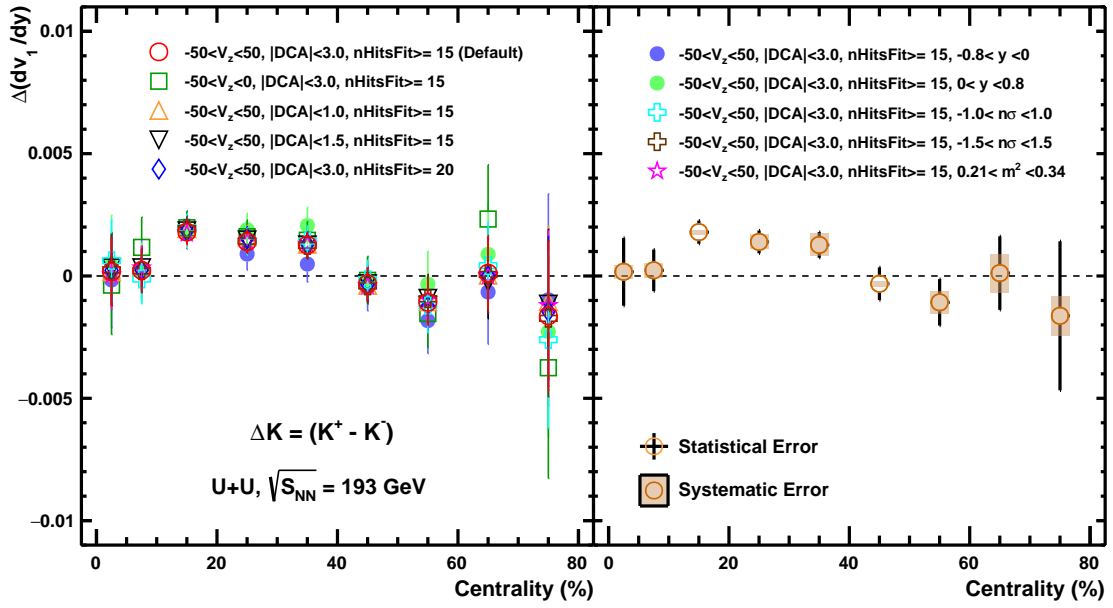


Figure 1-42 The $\Delta(dv_1/dy)$ of kaon for various systematic cuts (left panel) and the systematic/statistical error (right panel).

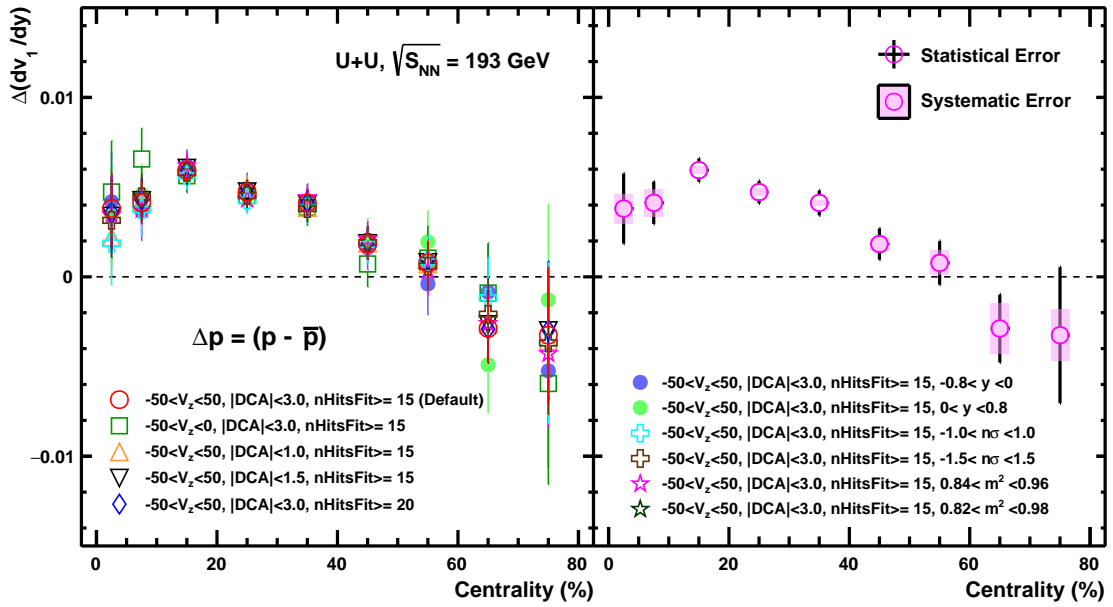


Figure 1-43 The $\Delta(dv_1/dy)$ of proton for various systematic cuts (left panel) and the systematic/statistical error (right panel).

1.7.4 Systematic Uncertainty of v_1 as a function of p_T

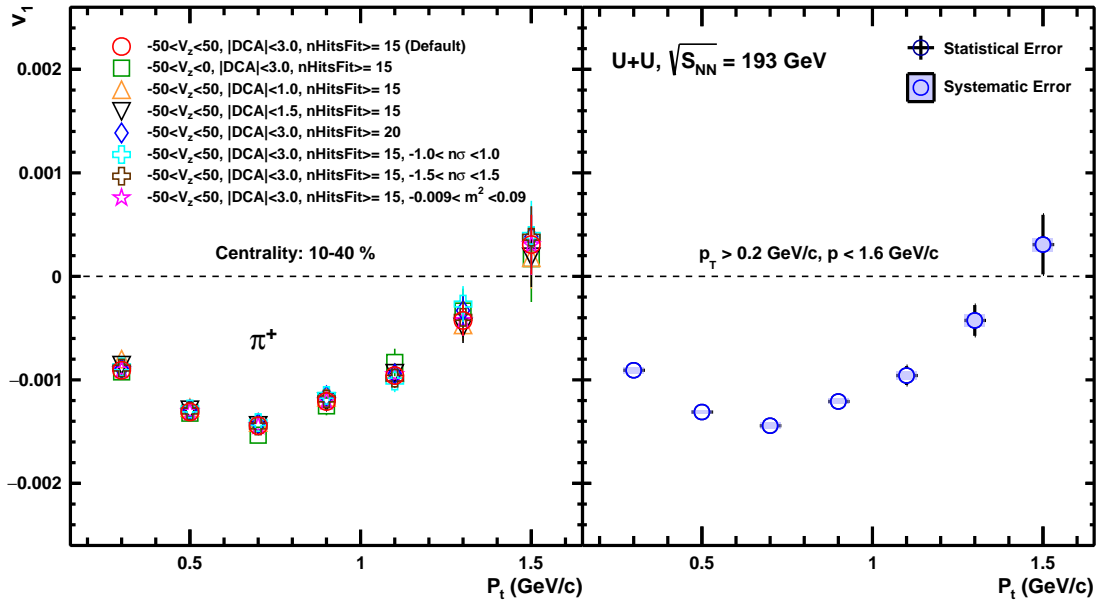


Figure 1-44 $v_1(p_T)$ of π^+ for various systematic cuts (left panel) and the systematic/statistical error (right panel) in 10-40% centrality.

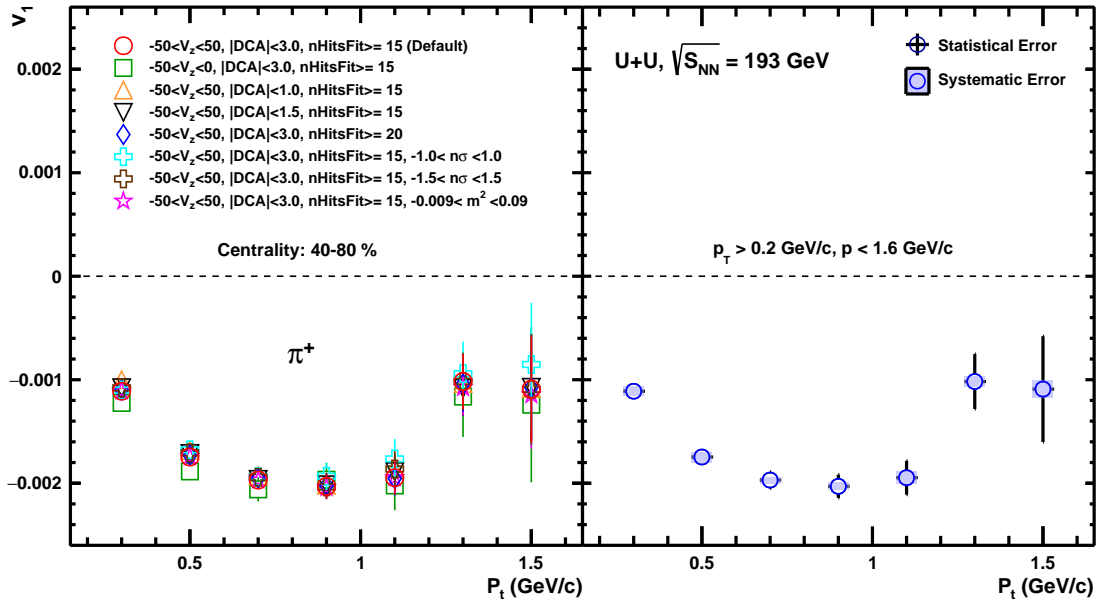


Figure 1-45 $v_1(p_T)$ of π^+ for various systematic cuts (left panel) and the systematic/statistical error (right panel) in 40-80% centrality.

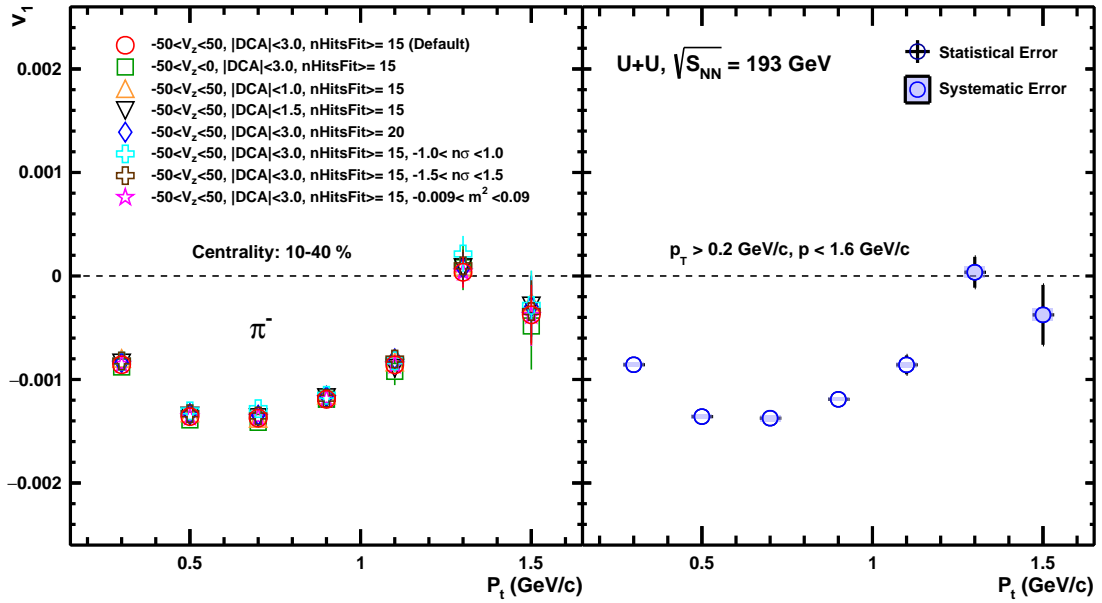


Figure 1-46 $v_1(p_T)$ of π^- for various systematic cuts (left panel) and the systematic/statistical error (right panel) in 10-40% centrality.

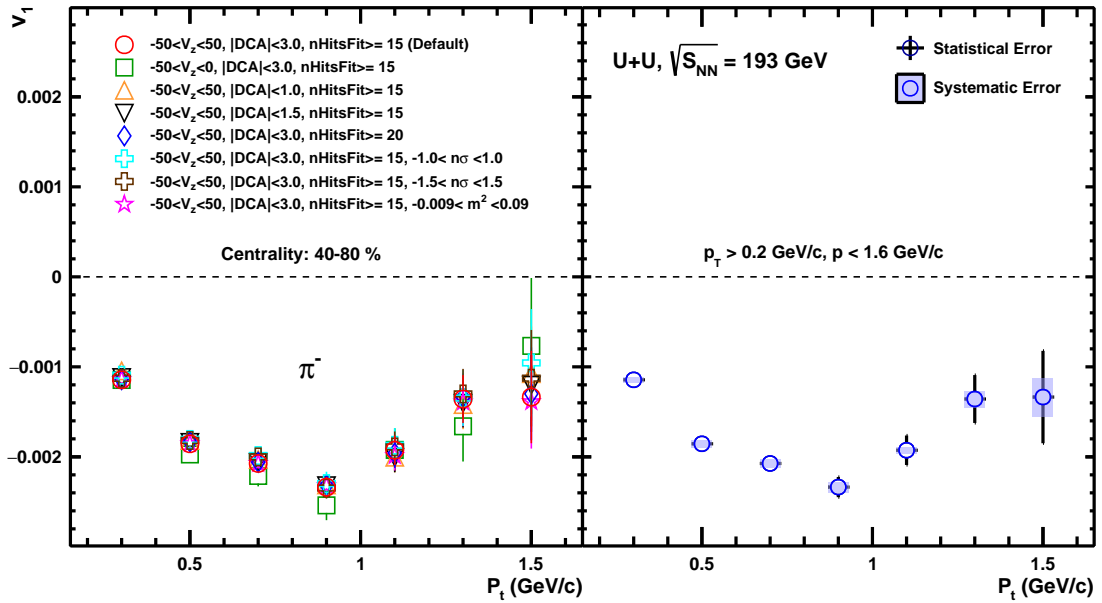


Figure 1-47 $v_1(p_T)$ of π^- for various systematic cuts (left panel) and the systematic/statistical error (right panel) in 40-80% centrality.

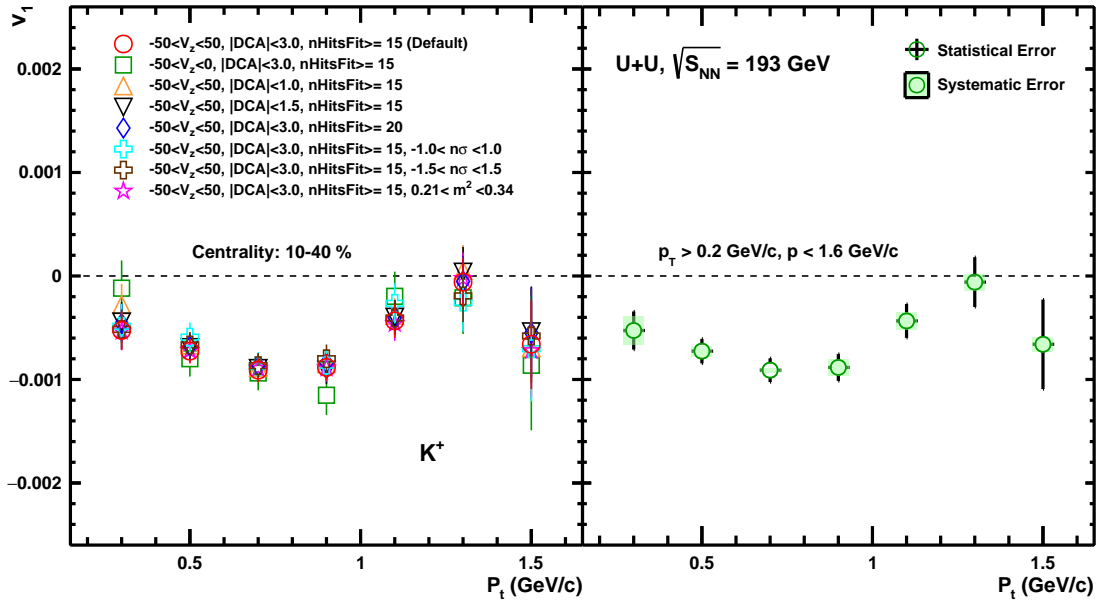


Figure 1-48 $v_1(p_T)$ of K^+ for various systematic cuts (left panel) and the systematic/statistical error (right panel) in 10-40% centrality.

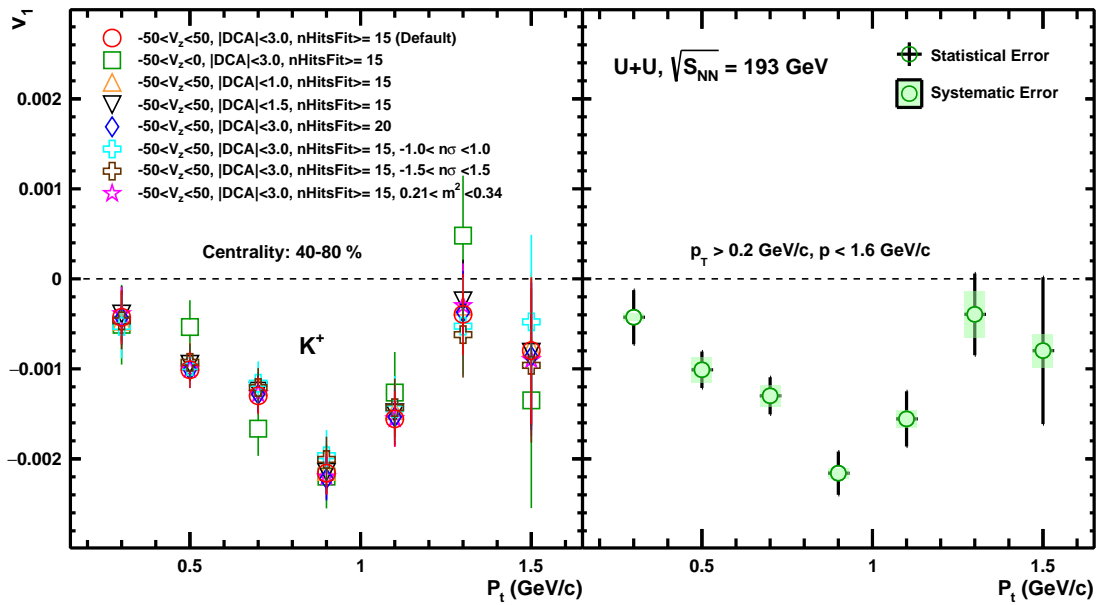


Figure 1-49 $v_1(p_T)$ of K^+ for various systematic cuts (left panel) and the systematic/statistical error (right panel) in 40-80% centrality.

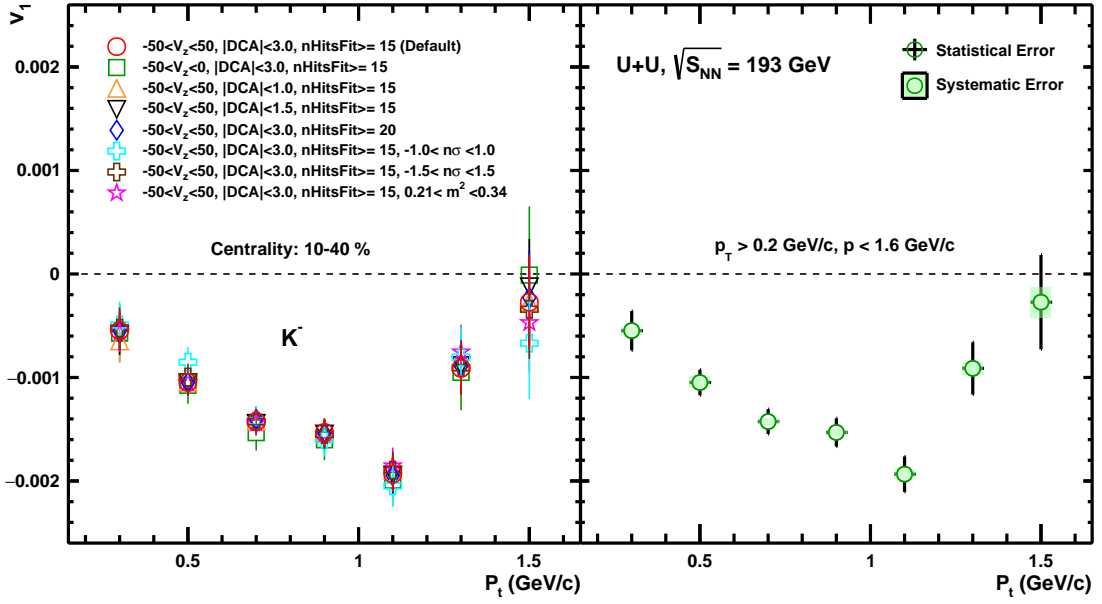


Figure 1-50 $v_1(p_T)$ of K^- for various systematic cuts (left panel) and the systematic/statistical error (right panel) in 10-40% centrality.

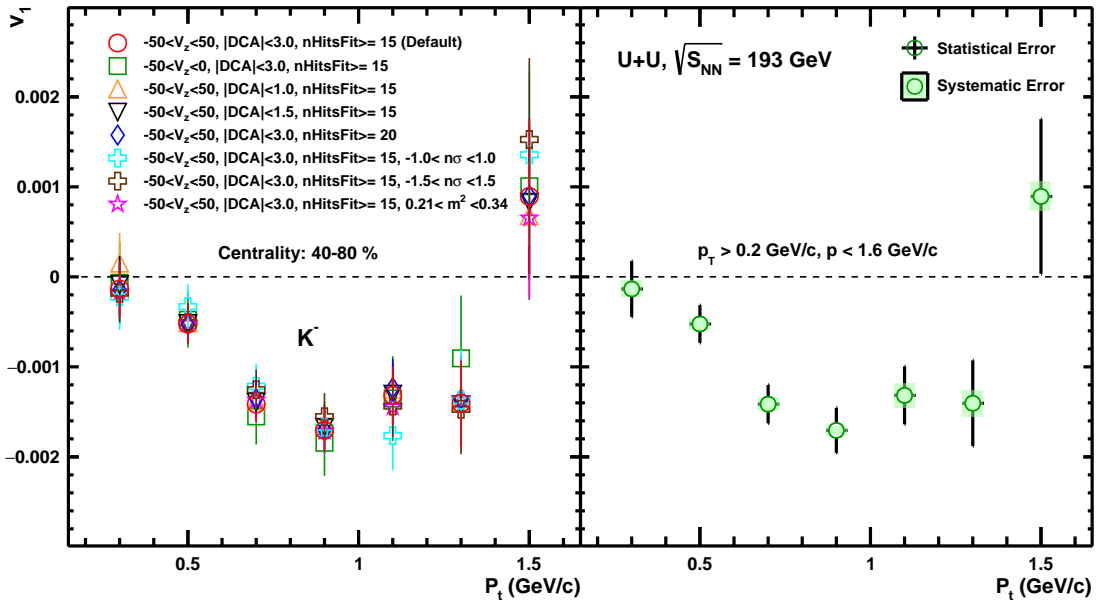


Figure 1-51 $v_1(p_T)$ of K^- for various systematic cuts (left panel) and the systematic/statistical error (right panel) in 40-80% centrality.

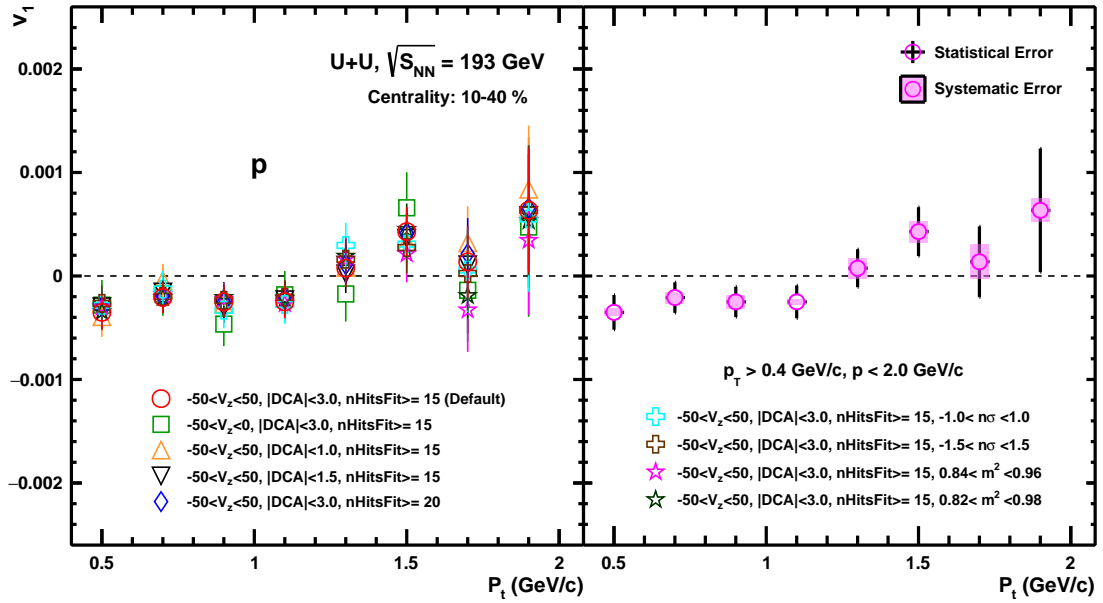


Figure 1-52 $v_1(p_T)$ of p for various systematic cuts (left panel) and the systematic/statistical error (right panel) in 10-40% centrality.

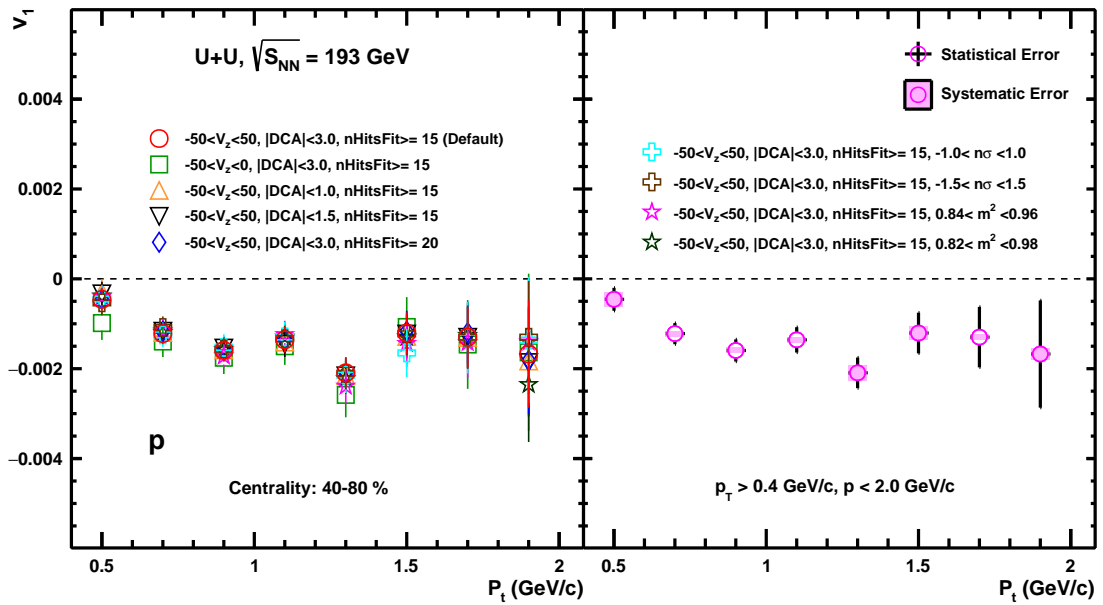


Figure 1-53 $v_1(p_T)$ of p for various systematic cuts (left panel) and the systematic/statistical error (right panel) in 40-80% centrality.

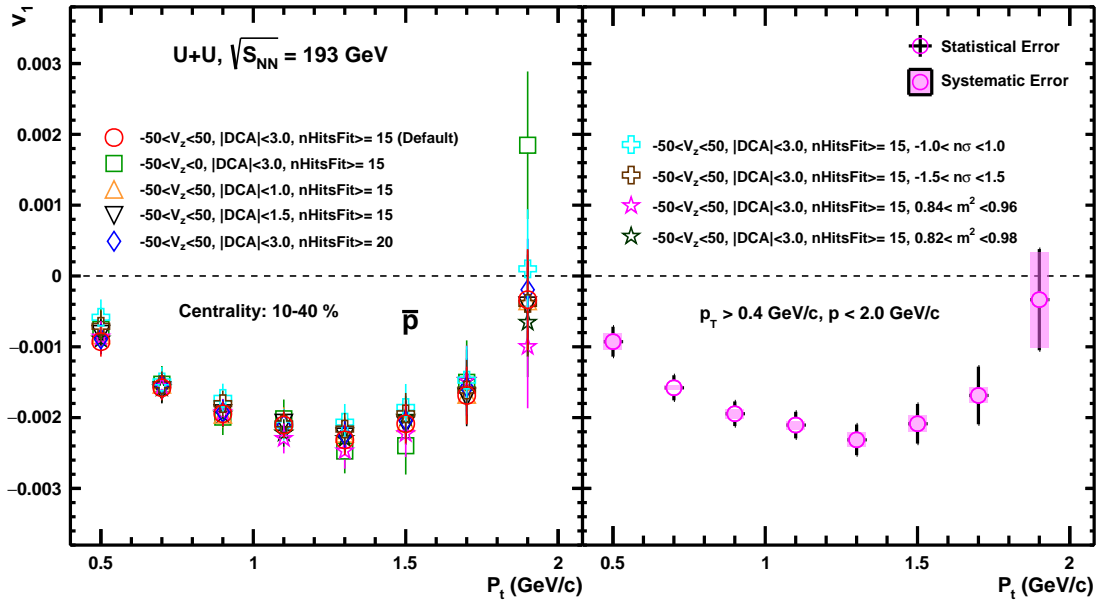


Figure 1-54 $v_1(p_T)$ of \bar{p} for various systematic cuts (left panel) and the systematic/statistical error (right panel) in 10-40% centrality.

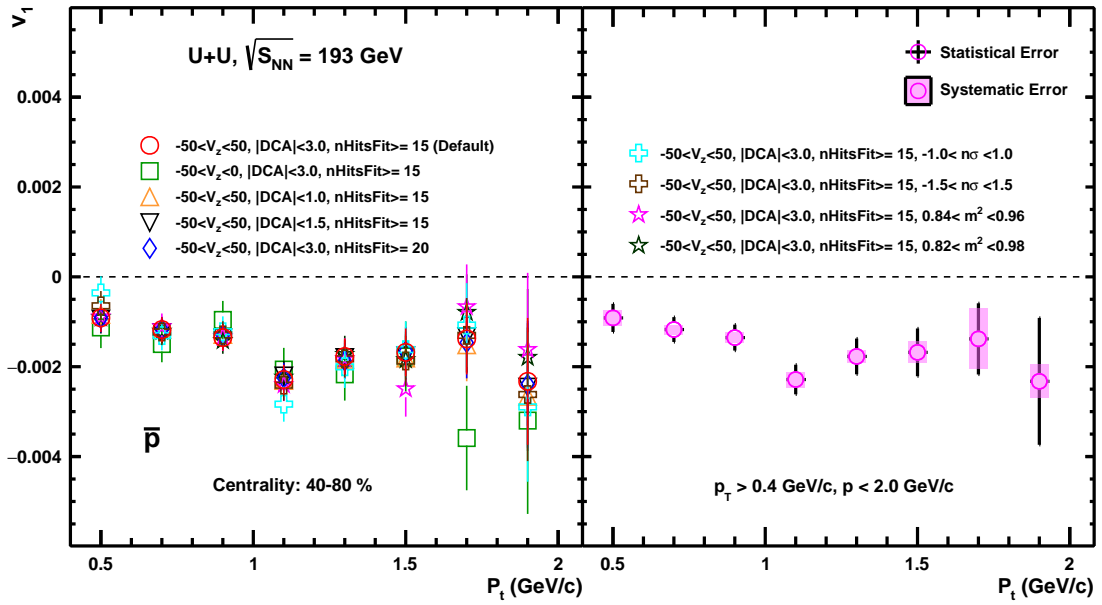


Figure 1-55 $v_1(p_T)$ of \bar{p} for various systematic cuts (left panel) and the systematic/statistical error (right panel) in 40-80% centrality.

1.8 Comparison of directed flow in U+U collisions at $\sqrt{s_{NN}} = 193$ GeV to Au+Au and Isobar (Ru+Ru and Zr+Zr) data at $\sqrt{s_{NN}} = 200$ GeV

In this section, we shall compare directed flow results of 193 GeV U+U collisions to those in Au+Au and Isobar (Ru+Ru and Zr+Zr) data at 200 GeV. In addition, the experimental data will be compared to Hydro Model at the end of this section.

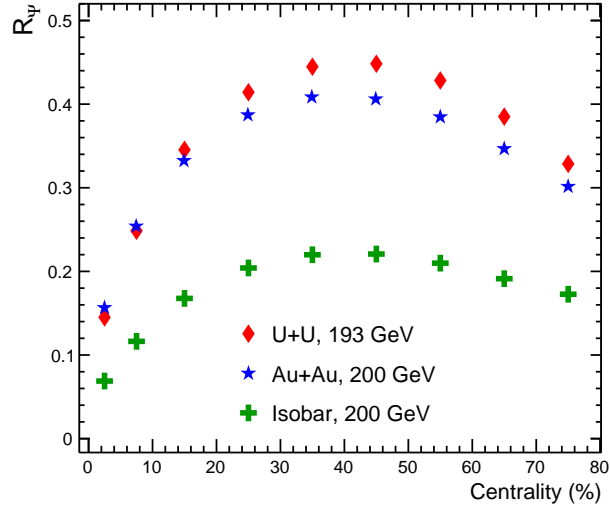


Figure 1-56 The event plane resolution as a function of centrality in U+U, Au+Au and Isobar (Ru+Ru and Zr+Zr) collisions at 193 and 200 GeV. The red marker is used for U+U, the blue marker is for Au+Au and the green marker stands for the resolution values in isobar data.

1.8.1 Directed flow of π^\pm in U+U, Au+Au and Isobar collisions

The comparison of directed flow as a function of rapidity for π^+ and π^- among the three different collisions systems is shown in figure 1.57. The slope dv_1/dy and the $\Delta(dv_1/dy)$ as a function of centrality between π^+ and π^- is compared in figure 1.58 and 1.59 respectively. It is observed that, for pions, the magnitude of v_1 , dv_1/dy as well as $\Delta(dv_1/dy)$ is same (within uncertainties) among the three different colliding species.

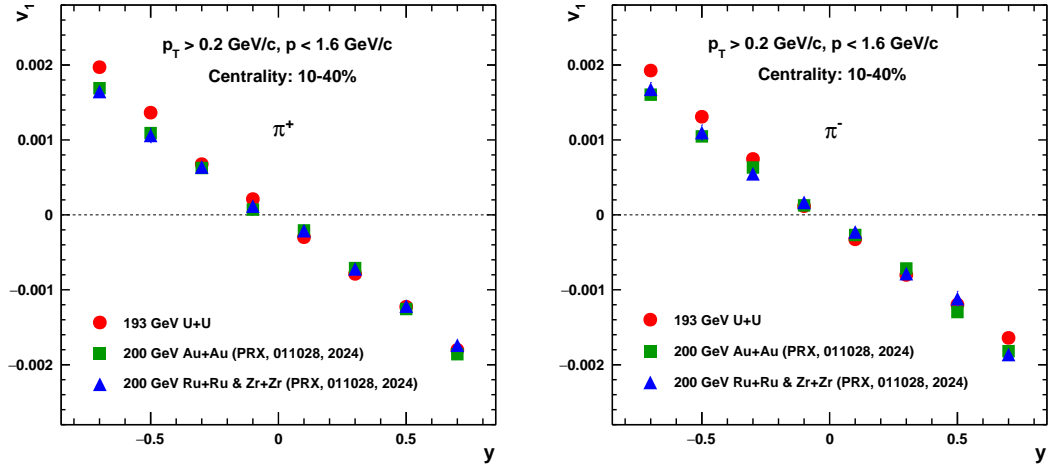


Figure 1-57 Comparison of directed flow of π^+ (left panel) and π^- (right panel) measured in this work with the published Au+Au and Isobar data at 200 GeV for 10-40% centrality.

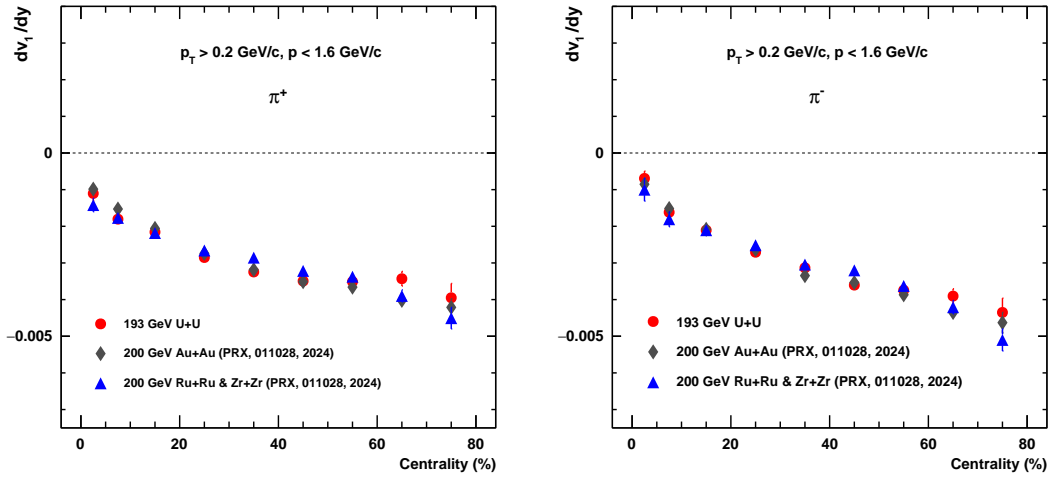


Figure 1-58 Comparison of slope (dv_1/dy) of π^+ (left panel) and π^- (right panel) measured in this work with the published Au+Au and Isobar data at 200 GeV.

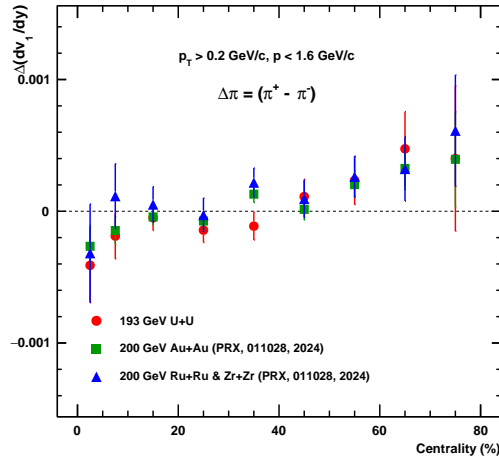


Figure 1-59 Comparison of $\Delta(dv_1/dy)$ of pion measured in this work with the published Au+Au and Isobar data at 200 GeV.

1.8.2 Directed flow of K^\pm in U+U, Au+Au and Isobar collisions

The directed flow of positive and negative charged kaons measured in this work is compared with published Au+Au and isobar (Ru+Ru and Zr+Zr) data as shown in figure 1.60, 1.61 and 1.62. The centrality dependent dv_1/dy and $\Delta(dv_1/dy)$ of kaons is found consistent (within uncertainties), similar to pions, among the different colliding systems.

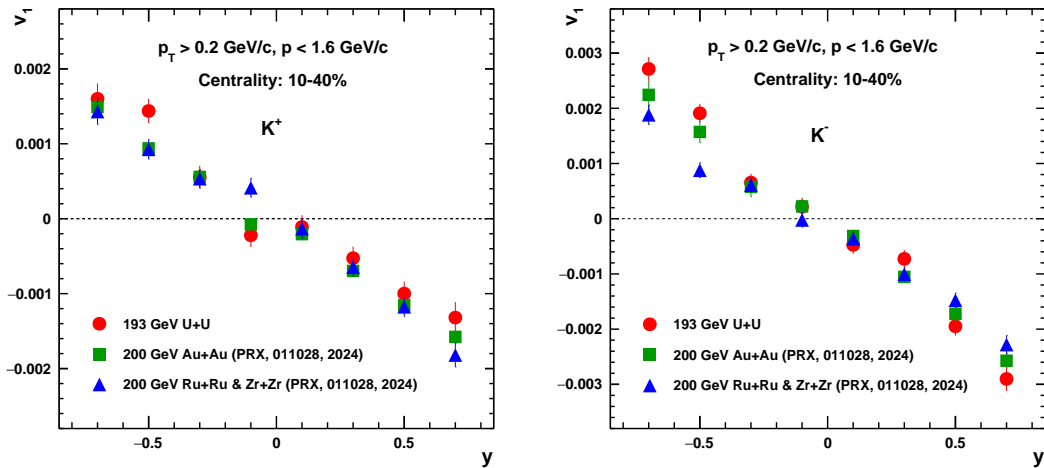


Figure 1-60 Comparison of directed flow of K^+ (left panel) and K^- (right panel) measured in this work with the published Au+Au and Isobar data at 200 GeV for 10-40% centrality.

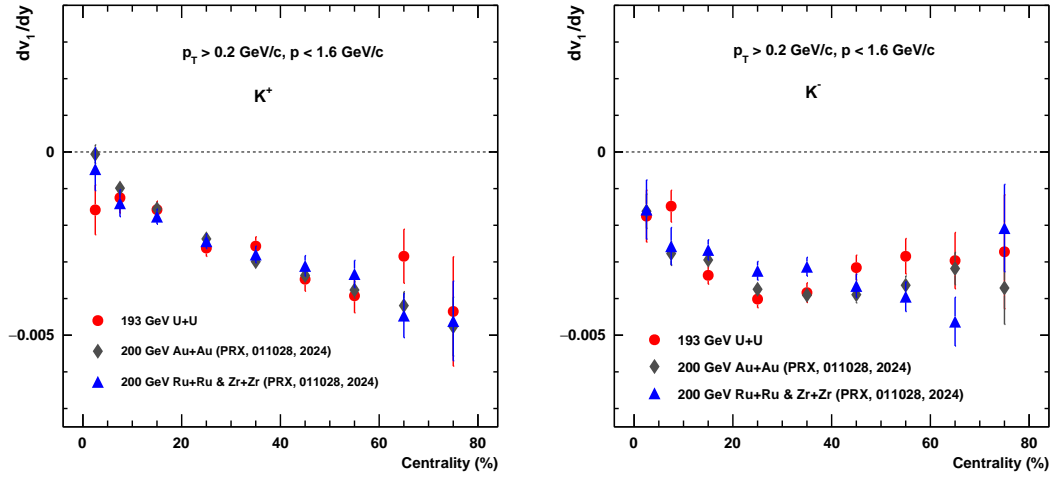


Figure 1-61 Comparison of dv_1/dy of K^+ (left panel) and K^- (right panel) measured in this work with the published Au+Au and Isobar data at 200 GeV.

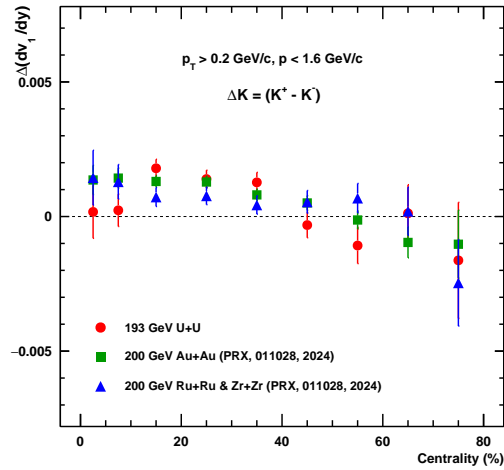


Figure 1-62 Comparison of $\Delta(dv_1/dy)$ of kaon measured in this work with the published Au+Au and Isobar data at 200 GeV.

1.8.3 Directed flow of p and \bar{p} in U+U, Au+Au and Isobar collisions

The comparison of directed flow of proton and antiproton in U+U, Au+Au and Isobar (Ru+Ru and Zr+Zr) systems will be presented in this section. Figure 1.63 shows the v_1 dependence on rapidity for p and \bar{p} in different collisions systems. A higher magnitude of v_1 (both in positive and negative rapidity bins) is observed in the published results as compared to v_1 measured in this work. The comparison of dv_1/dy and $\Delta(dv_1/dy)$ slope as a function of centrality is shown in figure 1.64 and 1.65 respectively. The dv_1/dy of proton shows a decreasing trend (from central to peripheral collisions) and it is true for all the three systems. For proton, the mid-central (10-40%) results of Δv_1 shows a system size dependence with a clear ordering among three different data presented in this report, whereas in the peripheral, it is difficult to distinguish between the data among three different systems due to large error bars.

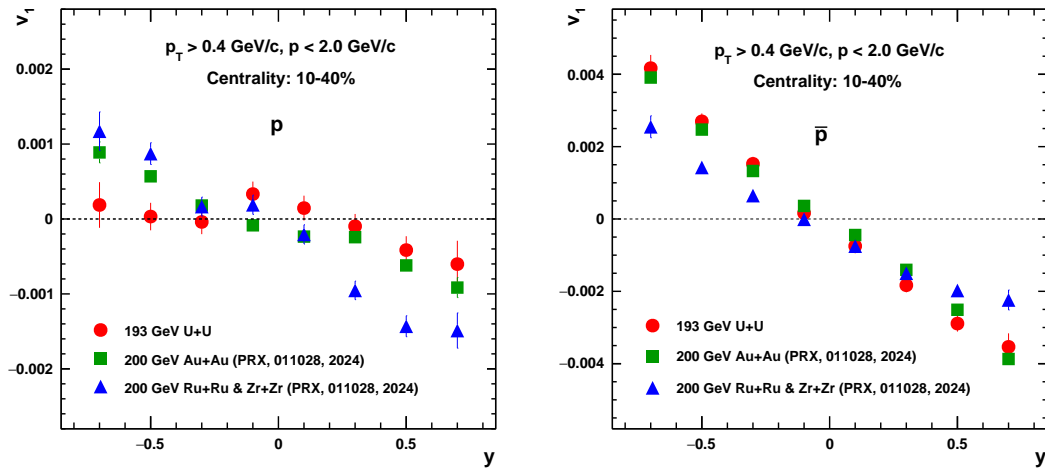


Figure 1-63 Comparison of directed flow of p (left panel) and \bar{p} (right panel) measured in this work with the published Au+Au and Isobar data at 200 GeV for 10-40% centrality.

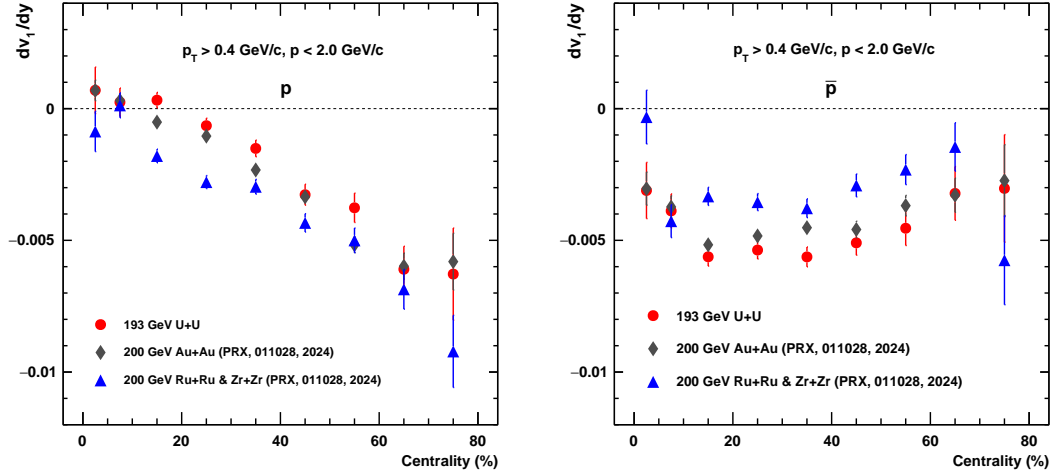


Figure 1-64 Comparison of dv_1/dy of p (left panel) and \bar{p} (right panel) measured in this work with the published Au+Au and Isobar data at 200 GeV.

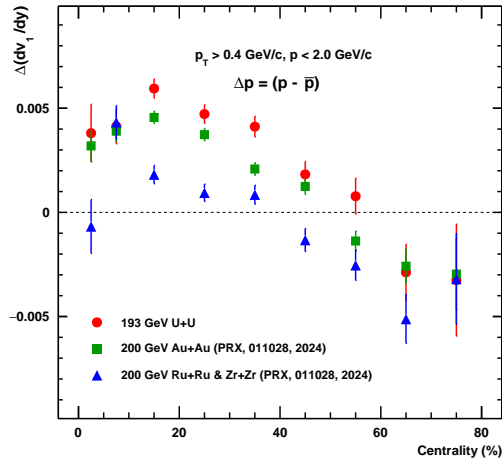


Figure 1-65 Comparison of $\Delta(dv_1/dy)$ of proton measured in this work with the published Au+Au and Isobar data at 200 GeV.

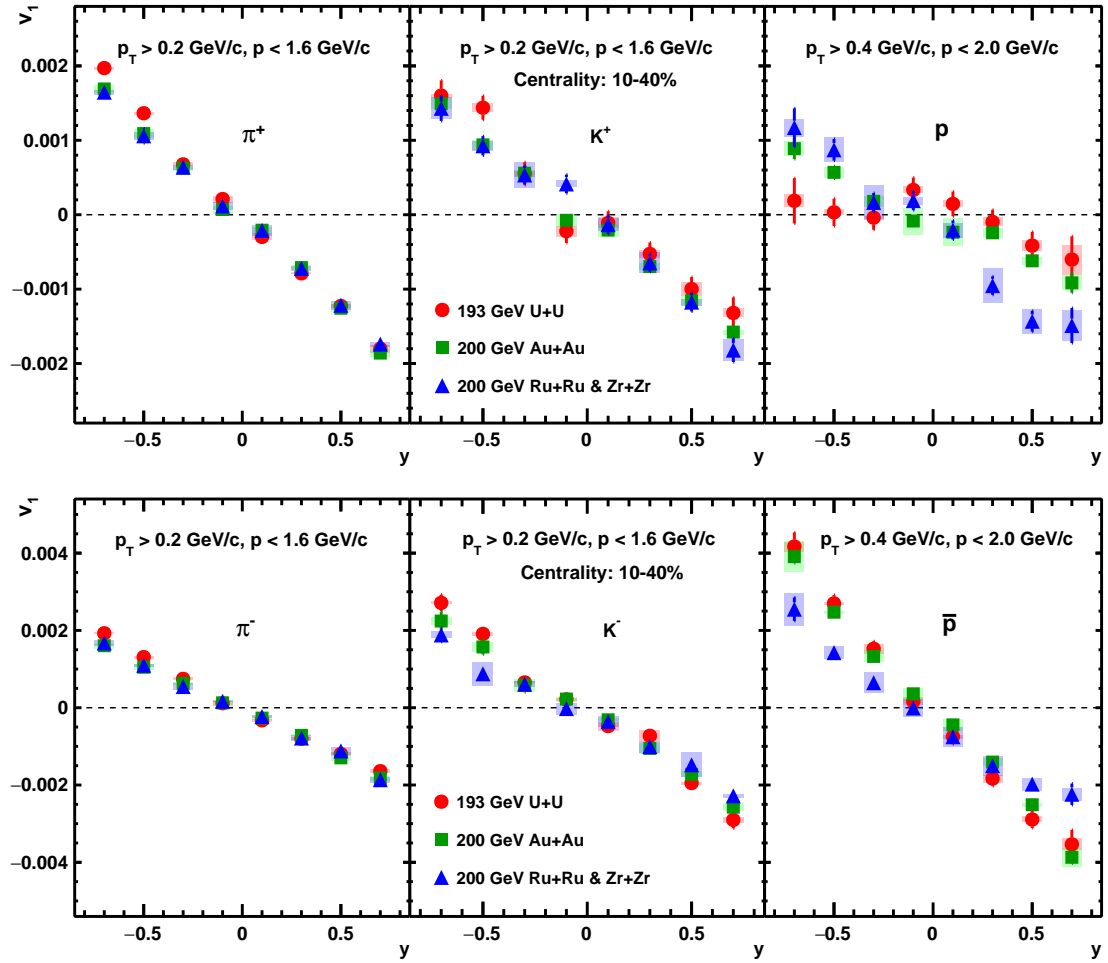


Figure 1-66 Plots show the directed flow (v_1) for π^\pm , K^\pm and $p(\bar{p})$ as a function of rapidity in U+U collisions at 193 GeV, Au+Au and Isobar (Ru+Ru and Zr+Zr) collisions at 200 GeV in 10-40% centrality. The red marker is used for U+U, green marker is for Au+Au and blue marker represents Isobar data. The shaded bands indicate systematic uncertainties.

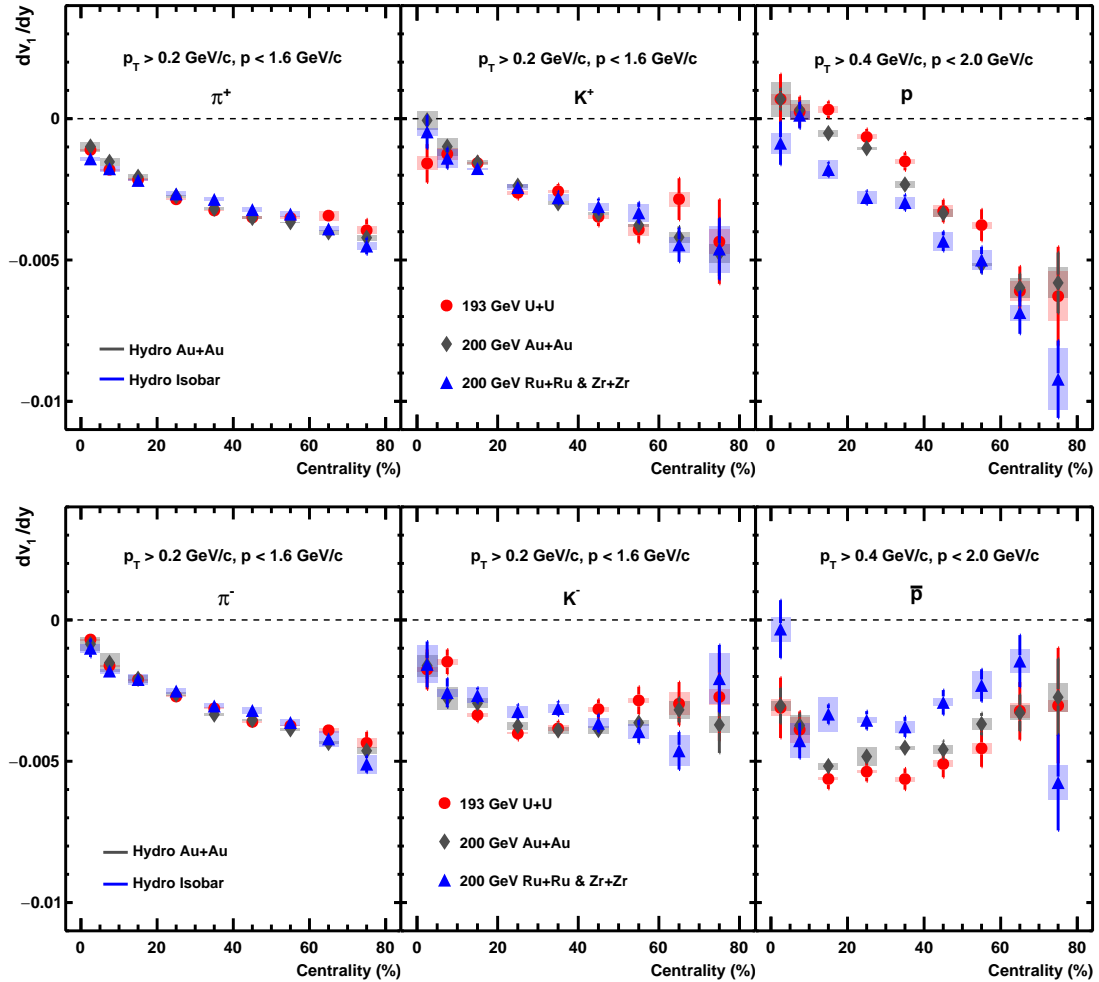


Figure 1-67 Plots show the slope (dv_1/dy) for π^\pm , K^\pm and $p(\bar{p})$ as a function of centrality in U+U collisions at 193 GeV, Au+Au and Isobar (Ru+Ru and Zr+Zr) collisions at 200 GeV. Slopes are obtained by fitting v_1 in $-0.8 < y < 0.8$ using a linear function. The red marker is used for U+U, black marker is for Au+Au and blue marker represents Isobar data. The Solid black and blue lines are the default hydro (inhomogeneous baryon distribution) model results for Au+Au and Isobar data respect. The shaded bands indicate systematic uncertainties.

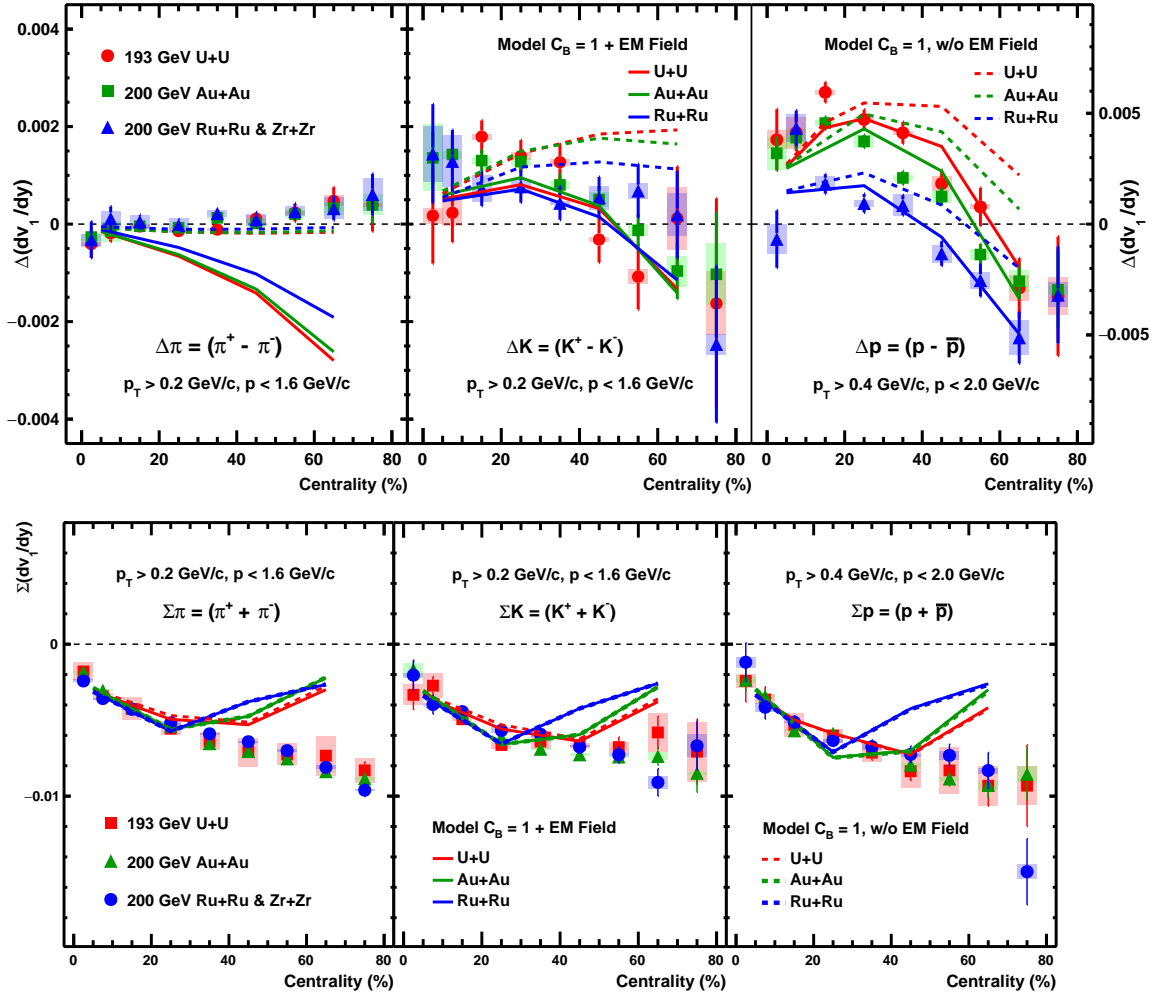


Figure 1-68 Plots show $\Delta(dv_1/dy)$ and $\Sigma(dv_1/dy)$ for π^\pm , K^\pm and $p(\bar{p})$ as a function of centrality in U+U collisions at 193 GeV, Au+Au and Isobar (Ru+Ru and Zr+Zr) collisions at 200 GeV. The red marker is used for U+U, green marker is for Au+Au and blue marker represents Isobar data. The Solid green and blue lines are the default hydro (inhomogeneous baryon distribution) model results for Au+Au and Isobar data. The dashed green line, in proton Δv_1 and Σv_1 , is a special case in which Au+Au hydro is run with net baryon same as Ru+Ru at a fixed $\langle N_{part} \rangle$. The shaded bands indicate systematic uncertainties.

1.9 Summary and Conclusion

The charge dependent directed flow (v_1) of pion, kaon and proton in U+U collisions at the nucleon-nucleon centre of mass energy 193 GeV is presented in this analysis using the data recorded by STAR experiment at RHIC. The observed Δv_1 slope between proton and anti-proton changes from positive in the central collisions to negative in the peripheral collisions. The positive Δv_1 for kaons and protons in central collisions can be attributed to the contributions from transported quarks, while the notable negative values observed in peripheral collisions are consistent with the effects of electromagnetic field, primarily due to Faraday induction combined with the Coulomb effect [1, 3].

For the first time, a clear signature of system size dependence of v_1 and Δv_1 for protons (antiprotons) is observed among the three different collision systems at the similar collision energy as shown in figures 1.67 and 1.68. In particular, the Δv_1 of proton is found proportional to the size of the colliding species in the semi-central collisions with an order of magnitude, $U+U > Au+Au > \text{Isobar (Ru+Ru and Zr+Zr)}$. Whereas, for pions, kaons as well as total baryons ($p + \bar{p}$), Δv_1 is found to be independent of system size, consistent with the previous studies at RHIC [2]. Additionally, the theoretical calculations using the default hydro model with an inhomogeneous baryon distribution (as shown in figures 1.67 and 1.68) can qualitatively capture the similar pattern of system size dependence of protons and antiprotons as we observed in the data. In a special case, when the Au+Au hydro is run with the net baryon same as Ru+Ru at a fixed $\langle N_{part} \rangle$, keeping all other parameters as default, proton Δv_1 shows no system size dependence especially in the central collisions as shown by green dotted lines in figure 1.68.

The influence of initial very strong electromagnetic fields as well as baryon transport in heavy ion collisions are the two possible mechanisms that can primarily induce the system size dependence of proton v_1 and Δv_1 . However, in the central collisions, where the dominance of electromagnetic fields is almost negligible, the baryon transport mechanism play its role in generating this Δv_1 pattern across different colliding systems. The results presented in this work will help to understand baryon deposition and provide strong constraint on baryon transport in heavy-ion collisions. Additionally, these results pave a way to investigate the strength and lifetime of the electromagnetic field and the medium electrical conductivity of the QGP in different collision systems.

Bibliography

- [1] Parida T, Chatterjee S. Baryon inhomogeneities driven charge dependent directed flow in heavy ion collisions [EB/OL]. 2023. <https://arxiv.org/abs/2305.08806>.
- [2] Abelev B I, Aggarwal M M, Ahammed Z, et al. System-size independence of directed flow measured at the bnl relativistic heavy-ion collider [J/OL]. Phys. Rev. Lett., 2008, 101: 252301. <https://link.aps.org/doi/10.1103/PhysRevLett.101.252301>.
- [3] Abdulhamid M I, Aboona B E, Adam J, et al. Observation of the electromagnetic field effect via charge-dependent directed flow in heavy-ion collisions at the relativistic heavy ion collider [J/OL]. Phys. Rev. X, 2024, 14: 011028. <https://link.aps.org/doi/10.1103/PhysRevX.14.011028>.
- [4] Gürsoy U, Kharzeev D, Marcus E, et al. Charge-dependent flow induced by magnetic and electric fields in heavy ion collisions [J/OL]. Phys. Rev. C, 2018, 98: 055201. <https://link.aps.org/doi/10.1103/PhysRevC.98.055201>.
- [5] Gürsoy U, Kharzeev D, Rajagopal K. Magnetohydrodynamics, charged currents, and directed flow in heavy ion collisions [J/OL]. Phys. Rev. C, 2014, 89: 054905. <https://link.aps.org/doi/10.1103/PhysRevC.89.054905>.
- [6] Sorge H. Elliptical flow: A signature for early pressure in ultrarelativistic nucleus-nucleus collisions [J/OL]. Phys. Rev. Lett., 1997, 78: 2309-2312. <https://link.aps.org/doi/10.1103/PhysRevLett.78.2309>.
- [7] Guo Y, Liu F, Tang A. Directed flow of transported and nontransported protons in au + au collisions from an ultrarelativistic quantum molecular dynamics model [J/OL]. Phys. Rev. C, 2012, 86: 044901. <https://link.aps.org/doi/10.1103/PhysRevC.86.044901>.
- [8] Nayak K, Shi S, Xu N, et al. Energy dependence study of directed flow in Au + Au collisions using an improved coalescence in a multiphase transport model [J/OL]. Phys. Rev. C, 2019, 100: 054903. <https://link.aps.org/doi/10.1103/PhysRevC.100.054903>.
- [9] Bożek P. Splitting of proton-antiproton directed flow in relativistic heavy-ion collisions [J/OL]. Phys. Rev. C, 2022, 106: L061901. <https://link.aps.org/doi/10.1103/PhysRevC.106.L061901>.